Magnetosphere-ionosphere coupling via prescribed field-aligned current simulated by the TIEGCM

A. Maute [1], A.D Richmond [1], G. Lu [1], D.J. Knipp[2], Y. Shi [3], B. Anderson[4]

[1]High Altitude Observatory, National Center for Atmospheric Research, Boulder CO, USA.

[2]University of Colorado, Boulder CO, USA.

[3]University of Michigan, Ann Arbor, USA.

[4]John Hopkins University/ Applied Physics Laboratory, Laurel, Maryland MD, USA.

Key Points:

- Present new approach to prescribe observed field-aligned current in the TIEGCM.
- Present technique to solve for interhemispherically asymmetric electric potential.
- The new approach increases the temporal TI-variation compared to empirical models.

Corresponding author: Astrid Maute, maute@ucar.edu

This is the author manuscript accepted for publication and has undergone full peer review but has not been through the copyediting, typesetting, pagination and proofreading process, which may lead to differences between this version and the Version of Record. Please cite this article as doi: 10.1029/2020JA028665.

Abstract

The magnetosphere-ionosphere (MI) coupling is crucial in modeling the thermosphere-ionosphere (TI) response to geomagnetic activity. In general circulation models (GCMs) the MI coupling is typically realized by specifying the ion convection and auroral particle precipitation patterns from e.g., empirical or assimilative models. Assimilative models, such as the Assimilative Mapping of Ionospheric Electrodynamics (AMIE), have the advantage that the ion convection and auroral particle precipitation patterns are mutually consistent and based on available observations. However, assimilating a large set of diverse data requires expert knowledge and is time consuming. Empirical models, on the other hand, are convenient to use, but do not capture all the observed spatial and temporal variations. With the availability of AMPERE data, there is an opportunity for employing field-aligned currents (FAC) in GCMs to represent the MI coupling. In this study, we will introduce a new method which enables us to use observed FAC in GCMs and solve for the interhemispherically asymmetric electric potential distribution. We compare Thermosphere-Ionosphere-Electrodynamics GCM (TIEGCM) simulations of a geomagnetic storm period using the new approach and two other often-used methods for specifying MI coupling based on empirical and assimilative high latitude electric potentials. The comparison shows general similarities of the TI storm time response and improved temporal variability of the new method compared to using empirical models, but results also illustrate substantial differences due to our uncertain knowledge about the MI coupling process.

Plain Language Summary

Our society is increasingly dependent on space assets for communication and navigation and ground infrastructures such as power grids and gas pipelines. The space environment is highly variable. Especially during geomagnetic storm large amount of energy enter Earth's upper atmosphere along field-lines from the magnetosphere and can drastically change the upper atmosphere, which can become hazardous for satellites and ground infrastructures. Numerical models are employed to simulate Earth's upper atmosphere during geomagnetic storms and describing accurately the coupling to the magnetosphere is crucial. In numerical models the coupling is typically realized by specifying the high latitude ion drift and auroral particle precipitation patterns from e.g., empirical or assimilative models. Assimilative models realistically describe the energy in-

put since they ingest available observations but they require expert knowledge to run. Empirical models are convenient to use and describe average conditions and do not necessarily capture all the observed variations. With the availability of observed field-aligned currents (FAC) there is the opportunity to represent the coupling via FAC. We introduce a new method using observed FAC in numerical models and compare results of a geomagnetic storm period using the new approach to using empirical and assimilative models for specifying coupling.

1 Introduction

Energy and momentum are transferred from the magnetosphere to the thermosphere-ionosphere (TI) system via the high latitude ionosphere. During geomagnetically active times, the electric and magnetic fields, as well as precipitation of energetic particles into the TI system, are significantly increased with complex temporal and spatial variations. The majority of the electromagnetic energy is dissipated in the TI system by Joule heating. This enhanced Joule heating rate leads to thermospheric expansion and to dynamical and compositional changes, and the scale sizes of such variations extend from local to global. High latitude electric fields change rapidly during geomagnetic storms, and a part of them can penetrate instantaneously to equatorial latitudes. In addition, ion-neutral coupling can stir up the neutral atmosphere at high latitudes and lead to disturbances in the neutral wind system, modifying the electrodynamics and composition, which in return influences the plasma distribution.

Even though there is an increased amount of ionospheric and thermospheric observations, e.g., from Global Positioning System Total Electron Content (GPS-TEC), Constellation Observing System for Meteorology, Ionosphere, and Climate (COSMIC), Global-scale Observations of the Limb and Disk (GOLD), Active Magnetosphere and Planetary Electrodynamics Response Experiment (AMPERE), general circulation models (GCMs) are needed to investigate the physical mechanisms responsible for the observed features. A major challenge in GCMs is still to describe the spatial and temporal variation of the MI-coupling (e.g., Heelis & Maute, 2020), particularly on smaller scale sizes (e.g., Nishimura et al., 2020), but also on large scales (larger than $\sim$ 300 km). In this study, we focus primarily on the large scale TI phenomena.

Several approaches exist to describe MI coupling in GCMs, such as coupling to global magnetohydrodynamic (MHD) magnetospheric models, using data driven assimilative methods and statistical/empirical models to quantify the high latitude forcing. In the following, we will briefly describe these approaches to highlight their differences.

Coupled models of the magnetosphere-ionosphere system, e.g., Space Weather Modeling Framework (SWMF) (Tóth et al., 2005), the Open Geospace General Circulation Model (OpenGGCM) (Raeder et al., 2001), the Coupled Magnetosphere-Ionosphere-Thermosphere (CMIT) model (Wiltberger et al., 2004), Grid Agnostic MHD for Extended Research Applications (GAMERA) (B. Zhang et al., 2019), have the advantage that the magnetosphere can respond to the ionosphere and vice versa (e.g., Wiltberger, 2015; Winglee et al., 2002). However, the coupled magnetosphere-ionosphere-thermosphere (MIT) models are complex and computationally expensive. As a result, the coupled MIT models are mostly used for case studies.

Another approach combines diverse sets of observations associated with MI coupling, e.g., ion drift, magnetic field perturbations, precipitation of auroral energetic particles, and assimilates them into mutually consistent global patterns of the electric potential, ionospheric current, and auroral energy flux and mean energy (e.g., Richmond, 1992; Cousins, Matsuo, & Richmond, 2015; Lu, 2017). In general, data assimilation methods are employed for case studies since data gathering and processing is a tedious, time-consuming task.

Often GCMs are driven by empirical models of the high latitude ion convection (e.g., Weimer, 2005; Heelis et al., 1982) and auroral particle precipitation (e.g., Roble & Ridley, 1987; Fuller-Rowell & Evans, 1987). The widely used Weimer ion convection model (Weimer, 2005) is derived from the Dynamic Explorer 2 (DE2) data set and parametrized by solar wind conditions and Earth's dipole tilt angle with respect to the Sun for opposite hemispheres. Empirical models are convenient to use since only a few parameters, e.g., the interplanetary magnetic field (IMF) and the dipole tilt, are required. Compared to the assimilative methods and coupled magnetosphere-ionosphere-thermosphere (MIT) models, empirical models describe the average high latitude ionospheric conditions that generally do not fully describe the actual spatial and temporal variations pertaining to a specific event. Interhemispheric asymmetry in empirical models (e.g., Weimer, 2005; Heelis et al., 1982) is simplified by reversing the signs of IMF B_y and Earth's dipole tilt

angle. Despite this limitation, empirical models are very helpful in understanding the general behavior of the TI system (e.g., Lei et al., 2015; Qian et al., 2014).

The Active Magnetosphere and Planetary Electrodynamics Response Experiment (AMPERE) project, following on earlier analysis of magnetic field measurements on board the 66 polar orbiting Iridium satellites, provides almost continuous magnetic field data from January 2010 (when data acquisition began) to August 2017 (current status) in the northern and southern polar regions. The field-aligned current (FAC) is derived from these magnetic field measurements. The Iridium constellation has a 9-min along track separation and approximately 2 hour local time (LT) separation (Anderson et al., 2000, 2002; Waters et al., 2001). The data processing is described by Anderson et al. (2014, and references therein). Spherical harmonic fitting is applied to obtain the polar FAC distribution, with a spatial resolution of 3^o in latitude and 2.4 hrs in local time (LT) every 2 min using a 10 min sliding window.

A series of studies highlight the value of the AMPERE data. The AMPERE FAC was used to examine magnetosphere-ionosphere coupling during geomagnetic storms and substorms (e.g., Anderson et al., 2005; Korth et al., 2005; Clausen et al., 2012; Shi et al., 2020b). The AMPERE data is also utilized to better describe high latitude ionospheric electrodynamics in assimilative methods by finding an optimal solution of the electric potential (e.g., Wilder et al., 2012; Yang et al., 2014; Lu et al., 2014; Lu, 2017) and of the magnetic potential (e.g., Matsuo et al., 2015; Cousins, Matsuo, & Richmond, 2015; Shi et al., 2020b). Solving the optimization problem directly for the magnetic potential has the advantage that no ionospheric conductivities need to be specified for the inversion (Matsuo et al., 2015). In the present study, FAC distributions based on that approach will be used. Details about the difference between FAC distributions from the AMPERE data product and the assimilative approach with respect to fitting functions and data gap filling are described by Matsuo et al. (2015).

At middle and low geomagnetic latitudes the electric potential is essentially constant along magnetic field lines, owing to the very large conductivity parallel to the magnetic field. Therefore, the potential is symmetric in geomagnetic coordinates between the northern and southern hemispheres. However, at high magnetic latitudes field lines extend far into the magnetosphere, where field-aligned electric fields can develop and where magnetic-field distortion associated with magnetospheric currents complicates the map-

ping of field lines between the two hemispheres. At these high latitudes hemispheric symmetry of the electric potential is no longer expected in magnetic coordinates which are normally determined by a geomagnetic field model that neglects magnetospheric influences on the tracing of field lines. In fact, notable asymmetry of the potential between the northern and southern polar caps has been found (e.g., Lukianova et al., 2008; Förster & Haaland, 2015; Pettigrew et al., 2010).

The FAC generally shows more interhemispheric asymmetry than does the electric potential. The FAC connects to the divergence of ionospheric currents flowing perpendicular to the geomagnetic field, which are associated with not only the electric potential but also with the conductivity and wind distributions, which have interhemispheric asymmetries of their own. At middle and low latitudes, where the potential is symmetric, the FAC is antisymmetric, because current flowing out of one hemisphere along a field line follows that field line into the opposite hemisphere. Differences in solar illumination between the hemispheres contribute to different conductivities, as do differences in magnetic field strength at conjugate points in the two hemispheres. Together with hemispheric asymmetry of the wind, interhemispheric asymmetry of the conductivity and of the high latitude electric field mean that the FAC generally is interhemispherically asymmetric everywhere. At high latitudes interhemispheric asymmetry of the FAC has been found by e.g., Fujii et al. (1981); Coxon et al. (2016); Cousins, Matsuo, Richmond, and Anderson (2015); Berchem et al. (2016). At low latitudes it has been examined by e.g., Fukushima (1979); Park et al. (2011); Lühr et al. (2015).

Numerical techniques exist to calculate the ionospheric electric potential from given distributions of conductivity, wind, and FAC from the magnetosphere under the condition that the electric potential is hemispherically symmetric everywhere, even in the polar cap (e.g., Richmond & Maute, 2014). In another approach, interhemispheric symmetry of the potential at middle and low latitudes is sometimes ignored, and the electric potential is solved for each hemisphere independently, based on conductivities, winds, and FAC for one hemisphere at a time, using simplified boundary conditions at low latitudes (e.g., Wiltberger et al., 2004; Tóth et al., 2005). No mutually consistent merging of these two approaches yet exists that takes into account the required low latitude symmetry and allows for high latitude asymmetry of the potential for a given FAC distribution, with physically appropriate boundary conditions at the equator and interface conditions between the polar and midlatitude regions.

The difficulty was illustrated by Marsal et al. (2012) who employed AMPERE field-aligned current to drive the NCAR Thermosphere-Ionosphere-Electrodynamics General Circulation Model (TIEGCM) and compared observed and simulated ground magnetic field variations. They demonstrated that the temporal variation of the simulated ground magnetic perturbations compared better with observations when prescribing AMPERE-FAC at high latitude instead of the empirical Heelis ion convection pattern (Heelis et al., 1982).

This issue of how to solve for interhemispheric asymmetry of the high latitude potential was addressed by Marsal et al. (2012) in an ad-hoc way by conducting three simulations with prescribed FAC from: 1. the northern polar region, 2. the southern polar region, and 3. the average of both. It was demonstrated that, depending on the location of the magnetometer station, one of the three simulations agreed better with the observations than the others. However, this approach cannot describe the thermospheric and ionospheric response to the interhemispherically asymmetric MI coupling in the ion drift, the plasma distribution, the dynamics, and the composition in a consistent way.

The goal of this study is thus to develop a method to include prescribed FAC in GCMs. We present an efficient way to incorporate observed FAC to improve on spatio-temporal variations in the TI system compared to empirical models. To our knowledge this is the first time that observed FACs are used in a thermosphere-ionosphere GCM to calculate the hemispherically different electric potential. The focus of the present study is on describing the new method and comparing it to other widely used MI coupling methods in GCMs.

We first provide an overview of the TIEGCM in Section 2, and then describe the ionospheric electrodynamics with prescribed high latitude potential in Section 2.1 and with prescribed FAC using the new approach in Section 2.2. In Section 3, we describe the set-up of the three simulations using Weimer electric potential, AMIE derived electric potential and particle precipitation, and high latitude observed FAC. The thermosphere-ionosphere response to geomagnetic activity of the three simulations is compared at high latitudes in Section 4 and in the middle and low latitude regions in Section 5. We summarize our findings in Section 6.

2 TIEGCM

The TIEGCM is a self-consistent numerical model of the thermosphere and ionosphere, which includes the dynamics, energetics and chemistry of the atmosphere and is coupled to a steady-state ionospheric electrodynamo. The original model development was done by Dickinson et al. (1984); Roble et al. (1988) and Richmond et al. (1992) and more information about the model updates can be found in Qian et al. (2014) and references therein. The TIEGCM ionospheric electrodynamo considers forcing by the wind dynamo, gravity and plasma pressure gradient driven current, and magnetosphere-ionosphere coupling (Richmond & Maute, 2013). In this study, we ignore the contributions from the gravity and plasma pressure gradient driven current. The model spans approximately from 97 km to 450–600 km depending on the solar cycle conditions.

In the default TIEGCM simulations, the high latitude energy input associated with auroral particle precipitation is represented by an analytical auroral model (Roble & Ridley, 1987; Emery et al., 2012) and the high latitude electric potential can be prescribed by the Weimer (2005) model. Alternatively, the auroral particle precipitation and potential patterns can be specified by the Assimilative Mapping of Ionospheric Electrodynamics (AMIE) procedure (e.g., Richmond, 1992) by ingesting various observations of, e.g., ion drift, magnetic perturbations, aurora energy spectrum. In this study, we introduce a third option of prescribing FAC based on observations.

2.1 Prescribed high latitude electric potential

The magnetosphere couples to the TI system at high latitude via the ionospheric electrodynamics. Therefore, we first provide the steady state electrodynamo equation based on a simplified version of Equation (11) from Richmond and Maute (2013), which considers a prescribed electric potential Φ^R pattern at high latitude.

$$p\frac{\partial}{\partial\phi_m}\left[\frac{\Sigma^T_{\phi\phi}}{\cos\lambda_m}\frac{\partial\Phi}{\partial\phi_m}+\Sigma^T_{\phi\lambda}\frac{\partial\Phi}{\partial|\lambda_m|}\right]+p\frac{\partial}{\partial|\lambda_m|}\left[\Sigma^T_{\lambda\phi}\frac{\partial\Phi}{\partial\phi_m}+\Sigma^T_{\lambda\lambda}\cos\lambda_m\frac{\partial\Phi}{\partial|\lambda_m|}\right]- \\ (1-p)\sigma^R R\cos\lambda_m\Phi = pR\left[\frac{\partial K^{DT}_{m\phi}}{\partial\phi_m}+\frac{\partial K^{DT}_{m\lambda}\cos\lambda_m}{\partial|\lambda_m|}\right]-(1-p)\sigma^R R\cos\lambda_m\Phi^R \tag{1}$$

with

λ_m, ϕ_m	modified apex latitude & longitude
R_E, h_R	Earth's radius and ionospheric reference height
$R = R_E + h_R$	Radius to the conducting ionospheric layer
$(\cdot)^N, (\cdot)^S, (\cdot)^{sym}$	northern, southern, and symmetric value
$(\cdot)^T$	sum of $(\cdot)^N$and $(\cdot)^S$
K^D	field-line integrated dynamo current term
Φ	electric potential
Σ	conductance term
σ^R, Φ^R	reference conductivity, prescribed electric potential
p	factor determines coupling strength of Φ to Φ^R

For the definition of the field-line integrated quantities K^D and Σ we refer to Richmond (1995) and Richmond and Maute (2013). The boundary conditions, in magnetic coordinates, are that the electric field is continuous in longitude and across the pole, and that the fieldline-integrated meridional current density vanishes at the equator.

The forcing via a prescribed electric potential Φ^R describes a perfect voltage generator for $p = 0$. The factor p and the reference conductivity σ^R determine the strength of the coupling of the potential Φ to the prescribed potential Φ^R. In the TIEGCM, p varies in magnetic latitude, being zero in the high latitude region where Φ^R is prescribed, one in the middle and low latitude region with pure wind dynamo forcing, and linearly varying in the transition region in-between. The transitional latitude of p from zero to one depends on the magnitude of the polar electric potential drop of Φ^R (see Supporting Information S1). The factor p is invariant in magnetic longitude. In the default TIEGCM, the northern hemisphere potential Φ^R is used when solving for Φ, which is hemispherically symmetric, i.e., the same at conjugate points in the two hemispheres. To account for interhemispheric difference in the high latitude electric potential, the southern hemisphere solution Φ is overwritten with the southern hemisphere prescribed potential Φ^R. Note that the low latitude "'penetration"' electric field effect, which generally is defined in the GCM as the instantaneous electric field without any wind dynamo present, is based on the northern hemisphere prescribed potential Φ^R. In the future it should be considered to modify the default TIEGCM to prescribe the hemispherically symmetric high

latitude electric potential with the associated "'penetration"' electric field effect, and then add or subtract the antisymmetric potential in the two hemispheres. In the high latitude region where $p = 0$, the wind dynamo is not considered explicitly in Equation (1).

2.2 Prescribed high latitude field-aligned current

In the following, we introduce the method to prescribe high latitude FAC in GCMs. This method essentially describes the MI coupling as a pure current generator in the absence of the wind dynamo. Note that when we use the term FAC in the following we refer to the radial component of the FAC associated with the convergence of transverse magnetospheric current along a field line.

In a first step, the electrodynamo equation is solved for an assumed hemispherically symmetric electric potential Φ^{sym} by forcing with the sum (or twice the interhemispherically symmetric part) of the prescribed FAC at conjugate points J_{Mr}. According to the notation by Richmond (1995) the magnetospheric source current along a field line is $J_{Mr} = J^N_{mr} + J^S_{mr}$. We add the superscript $(\cdot)^{sym}$ to the potential solution Φ to indicate that it is the symmetric response to the sum of the wind dynamo in both hemispheres and FAC density J_{Mr}.

$$\frac{\partial}{\partial\phi_m}\left[\frac{\Sigma^T_{\phi\phi}}{\cos\lambda_m}\frac{\partial\Phi^{sym}}{\partial\phi_m} + \Sigma^T_{\phi\lambda}\frac{\partial\Phi^{sym}}{\partial|\lambda_m|}\right] + \frac{\partial}{\partial|\lambda_m|}\left[\Sigma^T_{\lambda\phi}\frac{\partial\Phi^{sym}}{\partial\phi_m} + \Sigma^T_{\lambda\lambda}\cos\lambda_m\frac{\partial\Phi^{sym}}{\partial|\lambda_m|}\right] = R\left[\frac{\partial K^{DT}_{m\phi}}{\partial\phi_m} + \frac{\partial K^{DT}_{m\lambda}\cos\lambda_m}{\partial|\lambda_m|}\right] + J_{Mr}R^2\cos\lambda_m \tag{2}$$

In the second step, the residual FAC in each hemisphere $J^{N,res}_{mr}$ and $J^{S,res}_{mr}$ is determined by calculating the FAC that would be driven by Φ^{sym} and the conductivities and dynamo effects of that hemisphere, and subtracting it from the prescribed FAC $J^{N/S}_{mr}$. The hemispheric specific values are denoted by $(\cdot)^N$ and $(\cdot)^S$, or $(\cdot)^{N/S}$.

$$\begin{aligned} J^{N/S,res}_{mr} = & J^{N/S}_{mr} - \frac{1}{R^2\cos\lambda_m}\frac{\partial}{\partial\phi_m}\left[\frac{\Sigma^{N/S}_{\phi\phi}}{\cos\lambda_m}\frac{\partial\Phi^{sym}}{\partial\phi_m} + \Sigma^{N/S}_{\phi\lambda}\frac{\partial\Phi^{sym}}{\partial|\lambda_m|}\right] - \\ & \frac{1}{R^2\cos\lambda_m}\frac{\partial}{\partial|\lambda_m|}\left[\Sigma^{N/S}_{\lambda\phi}\frac{\partial\Phi^{sym}}{\partial\phi_m} + \Sigma^{N/S}_{\lambda\lambda}\cos\lambda_m\frac{\partial\Phi^{sym}}{\partial|\lambda_m|}\right] + \\ & \frac{1}{R\cos\lambda_m}\left[\frac{\partial K^{DN/S}_{m\phi}}{\partial\phi_m} + \frac{\partial K^{DN/S}_{m\lambda}\cos\lambda_m}{\partial|\lambda_m|}\right] \end{aligned} \tag{3}$$

The field-aligned current $J^{N/S,res}_{mr}$ represents the residual FAC, which effect is not captured by the hemispherically symmetric solution in Equation (2).

In a third step, we determine the electric potential in each hemisphere $\Phi^{N/S}$ due to the residual field-aligned current $J_{Mr}^{N/S,res}$ by solving the following equation separately for each hemisphere.

$$\begin{aligned} & p^c \frac{\partial}{\partial \phi_m}\left[\frac{\Sigma_{\phi\phi}^{N/S}}{\cos\lambda_m}\frac{\partial \Phi^{N/S}}{\partial \phi_m} + \Sigma_{\phi\lambda}^{N/S}\frac{\partial \Phi^{N/S}}{\partial |\lambda_m|}\right] + \\ & p^c \frac{\partial}{\partial |\lambda_m|}\left[\Sigma_{\lambda\phi}^{N/S}\frac{\partial \Phi^{N/S}}{\partial \phi_m} + \Sigma_{\lambda\lambda}^{N/S}\cos\lambda_m\frac{\partial \Phi^{N/S}}{\partial |\lambda_m|}\right] - (1-p^c)\sigma^c R\cos\lambda_m \Phi^{N/S} = \\ & p^c J_{mr}^{N/S,res} R^2 \cos\lambda_m - (1-p^c)\sigma^c R\cos\lambda_m \Phi^c \end{aligned} \tag{4}$$

We expect the residual field-aligned current $J_{mr}^{N/S,res}$ to be large in the high latitude region, and do not consider residual FAC in the middle and low latitude region. When solving for $\Phi^{N/S}$ we set the electric potential at middle and low latitude to zero by choosing $\Phi^c = 0$. The factor p^c depends on latitude and determines the transition latitude between specified potential and solving for $\Phi^{N/S}$. The factor p^c is zero at middle and low latitude and one at high latitude. We choose $p^c = 1$ poleward of $|\lambda_m| = 45^o$ and $p^c = 0$ equatorward of $|\lambda_m| = 40^o$. Therefore, the electric potential $\Phi^{N/S}$ will be zero equatorward of $|\lambda_m| = 40^o$, and is also set to zero over the entire opposite hemisphere. The regions where $\Phi^{N/S}$ are non-zero are unique for the corresponding hemisphere.

In a fourth step, the total potential is determined by adding the global potential solution from step 1 and the potential solution in each hemisphere from step 3

$$\Phi = \Phi^{sym} + \Phi^N + \Phi^S \tag{5}$$

For the present study, Equation 3 is not implemented in the precise form given. For computational simplicity, we approximate the hemispheric specific dynamo terms $K_{m\phi/\lambda}^{DN/S}$ by the sum of the dynamo terms in the two hemispheres $K_{m\phi/\lambda}^{DT}$ (see Richmond (1995) for definition), since at present the values of the hemispheric specific dynamo terms $K_{m\phi/\lambda}^{DN/S}$ are not easily available during the model computation, while those for $K_{m\phi/\lambda}^{DT}$ are. That is, we replace the wind-dynamo terms for each hemisphere by the sum of the value for both hemispheres. This simplification should give a reasonable approximation to the general properties of wind-dynamo effects on the polar potentials, if not a highly accurate representation. Since currents associated with the wind dynamo are generally much smaller than those associated with the electric field, this approximation introduces only relatively minor errors to the overall potential solution. Furthermore, when considering the combined wind dynamo forcing at high latitude, the errors tend to be antisymmetric between the hemispheres, so that their sum is small. During equinox conditions, the errors will

be further reduced in cases when the high latitude wind and conductivity patterns are not significantly different between hemispheres. We expect the magnitude of the errors to be roughly comparable to errors introduced by other approximations our technique utilizes, such as the lack of strict midlatitude conjugacy of the electric potential when Φ^N and Φ^S are added to Φ^{sym}.

In numerical TI models, the auroral particle precipitation and FAC distributions are often not derived in a mutually consistent way since they are based on measurements from different observational platforms and might use different parametrization (e.g., Marsal, 2015; Cousins, Matsuo, & Richmond, 2015; Zhu et al., 2020). In general, FAC mainly flows in regions with substantial Pedersen conductance. To avoid unreasonably large electric fields, we limit FAC flow into regions with low Pedersen conductance by adjusting the original FAC J_{mr}^{org} following Marsal et al. (2012) using

$$J_{mr}^{\Sigma} = \begin{cases} J_{mr}^{org} & \text{if } \Sigma_p > \Sigma_{\text{limit}}. \\ 0 & \text{if } \Sigma_p \leq \Sigma_{\text{limit}} \end{cases} \tag{6}$$

with the Pedersen conductance Σ_p and the conductance limit Σ_{limit}, which we have set to $\Sigma_{limit} = 1.5S$. Note that Marsal et al. (2012) used $\Sigma_{limit} = 2.0S$. The field-aligned current density at the top of the ionosphere integrated over the whole sphere has to vanish. We therefore adjust the prescribed non-zero field-aligned current $J_{mr,i}$ at location i by

$$J_{mr,i} = J_{mr,i}^{\Sigma} - \frac{\sum_{i=1}^{N}(J_{mr,i}^{\Sigma}\Omega_i)}{\sum_{i=1}^{N}\Omega_i} \tag{7}$$

subtracting the average residual from the local field-aligned current $J_{mr,i}^{\Sigma}$. The summations over all N points i in a hemisphere do not include the points with $J_{mr,i}^{\Sigma} = 0$ and their associated areas. This simple correction works for the examined time period in this study, but for other time periods it can lead to unrealistic electric field patterns. To avoid the distribution of field-aligned current into regions of low conductances, the adjustment should be weighted by the Pedersen conductance and the absolute magnitude of the field-aligned current as done by Marsal et al. (2012), in addition to adjusting the Σ_{limit} value.

3 Results

TIEGCM simulations using the new method of considering prescribed high latitude FAC will be compared to simulations employing the widely used method of prescribed high latitude electric potential patterns via the Weimer model and the AMIE procedure,

which are both briefly described in this Section. Because the high latitude electric fields, conductivities, and currents are different among the three techniques, ion drag and Joule heating are also different, resulting in different thermosphere and ionosphere responses to high latitude forcing. We focus on the ionosphere-thermosphere response to the simulated MI coupling during the 28-30 May 2010 period. It is important to point out that the analysis of this single time period is insufficient to allow us to draw general conclusions about the relative merits of the three ways of specifying high latitude inputs to the TIEGCM.

Figure 1 illustrates the IMF conditions for 28-30 May 2010 (day of year (DOY) 148 to 150), which was a modest storm with D_{st} reaching -80 nT on 29 May 2010 at 12 universal time (UT) when IMF B_z was southward for several hours (reaching -14nT) and IMF B_y is gradually rotated from negative to positive over the course of 29 May (DOY 149).

At the TIEGCM lower boundary (approximately at 97 km) all simulations specify tidal perturbations based on the Global Scale Wave Model (GSWM) tidal climatology (X. Zhang et al., 2010a, 2010b). GSWM includes the effect of migrating and non-migrating, diurnal and semidiurnal tidal components. The solar XUV, EUV (extreme ultraviolet), and FUV (far ultraviolet) spectral fluxes are defined by the EUV flux model for aeronomic calculations (EUVAC) (Richards et al., 1994) using the observed solar radio flux at 10 cm $F_{10.7}$.

3.1 Prescribing the field-aligned current

While it is possible to use the AMPERE FAC product as done by Marsal et al. (2012), we employ in this study the FAC distributions based on an assimilative method leading to latitudinally smoother variations (Matsuo et al., 2015) compared to the AMPERE FAC product. To derive the high latitude FAC in the two hemispheres, the magnetic field observations by Iridium satellites were processed as described by Shi et al. (2020a, 2020b). Information from 300 three-hour averages of AMPERE data allows the construction of a background model and creation of background error covariance matrix (Shi et al., 2020a), which in turn support an empirical orthogonal function analysis of the data. A small amount of data (in this case 4 min chunks of AMPERE data) updates the background via the optimal interpolation method to reconstruct the high-latitude magnetic potential and

FAC patterns at a specific time. The along-track magnetic perturbation data, which have larger uncertainties than the cross-track data, were included in the processing to improve the agreement of the total hemispherically integrated FAC magnitude compared to the AMPERE-FAC data product.

Using the observed magnetic perturbations, the mean and first five Empirical Orthogonal Functions (EOF) patterns of the magnetic potential are determined for a 3-hour time window. An Optimal Interpolation (OI) method is employed to derive the magnetic potential and FAC for a 4-min time window that slides in a 2-min cadence to get the time evolution. The procedure is restricted to the area poleward of 50^o magnetic latitude and provides the radial component of the FAC mapped to 110 km using Equation (7.3) in Richmond (1995). For details about OI method to derive FAC current patterns we refer to Shi et al. (2020a, 2020b). As mentioned in Section 2, the TIEGCM has a default analytical aurora model (Roble & Ridley, 1987; Emery et al., 2012) which is parametrized by the hemispheric power and the cross polar potential drop. Since the analytical aurora model and the FAC patterns were developed independently the location of the aurora does not necessarily align with the regions of prescribed FAC. Therefore, for the simulation with prescribed high latitude FAC, we modified the default auroral parametrization by increasing the aurora oval width and reducing the energy flux, decreasing the aurora oval offset toward midnight and increasing the offset toward dawn (see Table S1 in Supporting Information). This modification tends to lead to improved alignment of the prescribed FAC distribution with the auroral oval. An example of the auroral ionization rate distribution for 29 May 2010 (DOY 149) at 12 UT at approximately 118km is given in Figure 2. Details about the modifications can be found in the Supporting Information S1. For our plots we will use either quasi-dipole coordinates (which are nearly constant in height) or modified magnetic apex coordinates (which are constant along field lines) with a reference height of 90 km (for the electric potential) or 110 km (for the vertical current density). Note that quasi dipole and modified apex coordinates are similar in regions of almost vertical magnetic fieldlines and are identical if the quasi dipole height and the reference height are the same (Richmond, 1995). In the following, we abbreviate the simulation with prescribed FAC by OIM-FAC to point out that the FAC is obtained by the Optimal-Interpolation Method (OIM).

3.2 Prescribing the Weimer electric potential

For comparison, we also simulate the time period using at high latitude Weimer electric potential pattern parametrized by IMF B_y and B_z, solar wind density and velocity, and dipole tilt angle. The solar wind data used in the TIEGCM has a 5-min cadence and is linearly interpolated to the model time. The TIEGCM default aurora parametrization for the Weimer case is employed as shown in Supporting Information S1 (Emery et al., 2012). In Figure 2 the default auroral ionization rate distribution for the Weimer case (left panel) illustrates higher ionization rates over a smaller area than for the OIM-FAC case (right panel) due to the modified aurora parametrization described in Section 3.1. The transition latitude from specified electric potential to solving for the potential due to the wind dynamo varies with the strength of the average northern and southern hemisphere electric potential drop (see Supporting Information S1 for details). In the following, we abbreviate the simulation with prescribed Weimer electric potential by Weimer-POT.

3.3 Prescribing AMIE electric potential and auroral particle precipitation

In addition, we simulate the time period using electric potential and aurora particle precipitation patterns derived from the AMIE procedure (Lu et al., 2001). For this event, the data inputs to AMIE are ground magnetic perturbations from 185 magnetometer stations, the Super Dual Auroral Radar Network (SuperDARN) line-of-sight ion drift, the AMPERE magnetic field, and ion drifts from DMSP (F15, F16, and F18) as well as auroral precipitation from DMSP/SSUSI (F16, F17, and F18) to derive an optimal fit of ion convection and particle precipitation. In data sparse regions, the fitting relies heavily on statistical information from the background models. AMIE provides mutually consistent global patterns of electric potential and auroral energy flux and mean energy in both northern and southern hemispheres every 5 mins. Since the AMIE patterns are based on more observations, we expect that the TIEGCM simulation with AMIE forcing includes spatial and temporal details not captured by the Weimer-POT and different from the OIM-FAC simulations. The auroral ionization rate in Figure 2 based on AMIE (middle panel) includes more spatial structure than presented in the analytical model used in the TIEGCM (left and right panel). The two auroral ionization rate distributions based on the analytical model in Figure 2 do not agree since the parametrization differs as de-

scribed in Section 3.1 In the following, we abbreviate the simulation using AMIE patterns by AMIE-POT.

4 Comparison in the high latitude region

In this Section, we compare the three simulations in the high latitude region to assess the TIEGCM simulation with prescribed FAC in general terms. First, we compare the FAC distribution at DOY 149 (29 May 2010) at 12 UT in Figure 3 from the AMPERE-FAC data product, the empirical Weimer FAC model (Weimer, 2005), the AMIE procedure, and the OIM-FAC used in this study (see Section 2). Except for the Weimer FAC model (Fig. 3b) all other distributions (Fig. 3a, 3c, 3d) are based on AMPERE observations. The AMIE procedure, however, ingests additional data. The processing of the magnetic perturbations to derive the AMPERE-FAC data product (Fig. 3a) and the OIM-FAC (Fig. 3d) differs, leading to some deviations in the FAC patterns. The AMPERE-FAC data product has more spatial structure, especially in latitudinal direction, which might be an artifact of the spherical harmonic analysis (e.g., Marsal et al., 2012; Matsuo et al., 2015). Both the FAC density from OIM-FAC case and from AMIE tend to be smoother than the AMPERE-FAC data product.

In general, the maximum region-2 current in the OIM-FAC case tends to be smaller than that in the AMIE case and in the AMPERE-FAC data product. The AMIE-FAC patterns include more detailed structures such as the upward current around midnight which are also in the AMPERE-FAC data product, but not captured by Weimer-FAC and OIM-FAC. The empirical FAC model by Weimer (2005) is parametrized in a similar way as the associated empirical electric potential model, and based on Dynamic Explorer-2 (DE2) magnetic perturbations to derive the magnetic potential. The region-1 current of the Weimer-FAC is distributed over a wider latitudinal range and the region-2 current of the Weimer-FAC is more equatorward than in the other cases. Overall, the FAC distributions of the different cases are reasonable and representative for the southward IMF conditions.

The integrated upward field-aligned current density poleward of quasi dipole latitude $\lambda_q = 50^o$ is illustrated in Figure 4. During the quiescent day (DOY 148) the integrated FAC from the AMPERE data product, AMIE-FAC and OIM-FAC agree very well. The integrated FAC from the Weimer FAC model is mostly larger than those from

the other cases. The temporal variation of the integrated Weimer FAC tends to be smoother than for the other three cases, particularly during the disturbed day 149.

The magnitude and temporal variation of the AMPERE-FAC and AMIE-FAC agree best with each other. Note that the AMIE procedure ingests the AMPERE data. The OIM-FAC (red lines) tends to underestimate the integrated FAC during the geomagnetically active time, more so in the southern than in the northern hemisphere. The reduced magnitude of region-1 and region-2 current of the OIM-FAC case compared to AMIE-FAC and the AMPERE-FAC data product is also visible in Figure 3. The comparison suggests that the data processing in the OIM-FAC case reduces the FAC magnitude, but on the other hand leads to smooth, well behaved spatial FAC variations, which fit reasonably well to the TIEGCM auroral particle precipitation. Since the focus of this study is on presenting the new method, we do not artificially increase the magnitude of OIM-FAC.

The simulated total radial current density is illustrated in Figure 5 due to high latitude forcing and wind dynamo, and in Figure 6 due to the wind dynamo alone (convergence of transverse wind dynamo current along a field line) for the same time as the field-aligned current density in Figure 3. In the case of driving the TIEGCM with OIM-FAC we expect that the FAC (Fig. 3d) (note that this is the radial component of the FAC) is very similar to the total simulated radial current density (Fig. 5c) since we prescribe the field-aligned current density in high latitude region. Some minor difference can exist due to the adjustment of the FAC described in Section 2.2.

When we prescribe a high latitude electric potential pattern in the TIEGCM the wind dynamo does not affect the potential solution poleward of θ_{cp} (see Supporting Information S1) as described in Equation (1). But, the total current in Figure 5 does include the wind dynamo driven FAC. The radial current density due to the wind dynamo (Figure 6) tends to be opposite to the FAC (Figure 3) (Lu et al., 1995), which contributes to the fact that the simulated total radial current density (Figure 5b) for the AMIE-POT case is reduced compared to FAC from the AMIE procedure in Figure 3c.

The difference between the Weimer empirical FAC model in Figure 3b and the simulated total radial current density in Figure 5a is larger than that for the AMIE and OIM-FAC cases. The magnitude and latitudinal variation of the simulated radial current density (Figure 5a) agrees better than the empirical Weimer FAC model with the FAC dis-

tributions from the AMIE-POT and OIM-FAC cases. While the empirical FAC represents average conditions, the simulated radial current density is strongly influenced by the modeled auroral conductivities, leading to a more confined current density compared to the empirical FAC model, which highlights the importance of the auroral conductivities.

The wind driven radial current densities of the three cases (Figure 6) are similar, indicating that the neutral wind and the conductivities have overall similar variations in the three cases. The dynamo driven radial current density from the AMIE-POT and OIM-FAC cases are similar in both magnitude and overall distribution. There are some differences in the southern hemisphere around 3 magnetic local time (MLT) and noon time. Note that for the AMIE-POT case, AMIE provides mutually consistent auroral particle precipitation while for the OIM-FAC case the TIEGCM analytical aurora model with modified parametrization is used. The difference in auroral ionization (indicated in Figure 2 at 118km) combined with differences in the neutral wind (indicated in the zonal mean wind in Figure 10) can lead to these differences in the wind driven FAC. The dynamo driven radial current density is in general larger in the Weimer-POT case than in the other two cases, especially toward the equatorward edge of the aurora. This can partly contribute to the more confined total radial current density pattern (Figure 5a) at high latitude compared to the empirical Weimer FAC model (Figure 3b).

The cross polar potential drop is roughly a measure of the strength of the electric field, especially during periods dominated by two-cell convection patterns. The temporal variation of the electric potential drop in the northern and southern polar region is depicted in Figure 7, indicating better agreement in magnitude and temporal variation between the AMIE-POT and OIM-FAC potential drop than between the AMIE-POT and Weimer-POT cases. For the Weimer-POT case, the potential drop is in general larger than that for the other two cases, and the magnitude of the variation tends to be dominated by the IMF B_z variation.

The spatial variations of the electric potential are compared in Figure 8 for 29 May 2010 (DOY 149) at UT 12, when southward IMF B_z dominates. For comparison the SuperDARN assimilative mapping (SAM) (Cousins et al., 2013) of the electric potential is added (Figure 8a) based on ion drift measurements by SuperDARN. The ion drift observations are shown by the colored arrows in Figure 8a. The SAM background model is based on the SuperDARN observations.

The Weimer polar potential drop is up to 50% larger than that for the AMIE-POT and OIM-FAC cases (see Figure 7). The SuperDARN and the Weimer potentials represent a more symmetric two-cell pattern. The AMIE potential, which is partly informed by SuperDARN data, is more distorted. The electric potential is solved for in the OIM-FAC case (not prescribed as for Weimer-POT and AMIE-POT cases), and therefore also depends on the aurora conductance. Any misfit between the spatial variation of the FAC and auroral particle precipitation can result in unrealistic electric potential variations. In the OIM-FAC case (Figure 8d), there is a secondary minimum in the southern hemisphere around 4 MLT and $\lambda_m = -60^o$ which could be caused by such a misfit. Overall, the electric potential for the OIM-FAC case has a smooth structure and the potential drop strength is in reasonable agreement with the one from the AMIE-POT case with some difference in the pattern's morphology.

The hemispherically integrated Joule heating rate is often used as a measure of the energy input from the magnetosphere into the ionosphere. The hemispherically integrated Joule heating rate poleward of $\lambda_q = 50^o$ is given in Figure 9 for the 3 simulations. During the active day on 29 May 2010 (DOY 149) the Joule heating rate for the Weimer-POT case is significantly larger than that for the AMIE-POT and OIM-FAC simulations. Note that for all TIEGCM simulations, the Joule heating rate is increased by 50% to account for small scale electric field variability not captured by the large scale electric field and auroral precipitation (e.g., Codrescu et al., 1995). Similar to the potential drop variation, the Joule heating rate of the Weimer-POT simulation tends to correlate directly with the IMF B_z variations (Figure 1), which causes a single spike of 400 GW at the end of DOY 149 due to the sudden southward turning of B_z. This spike is much smaller in the AMIE-POT and OIM-FAC simulations. The temporal variability and interhemispheric differences in the hemispherically integrated Joule heating rate during DOY 149 are more prominent for the AMIE-POT and OIM-FAC cases than for the Weimer-POT case.

Overall, the hemispherically integrated Joule heating rate from the OIM-FAC simulation tends to track that from the AMIE-POT simulation reasonably well. There are some differences during the first few hours of DOY 149 when the northern hemisphere Joule heating rate from the OIM-FAC case is as large as that from the WEIMER-POT case and almost double that from the AMIE-POT case. This is associated with the larger potential drop in the OIM-FAC case compared to the AMIE-POT simulation during that time period (Figure 7). Similarly, around 7 UT on DOY 149 (149.3), the OIM-FAC in-

tegrated Joule heating dips below the AMIE-POT Joule heating due to the smaller polar potential drop (Figure 7). The southern hemisphere Joule heating rate from the OIM-FAC case tends to be lower than that from the AMIE-POT simulation, but the Joule heating rate difference is not as large as the difference between the AMIE-POT and Weimer-POT cases. Note that for the Weimer-POT and AMIE-POT cases, the Joule heating rate scales with the Pedersen conductance since the electric field is prescribed, but in the OIM-FAC case, the relationship is more complex since any increase/decrease in the polar conductance tends to be balanced by a decrease/increase in the electric field to maintain the prescribed FAC.

5 Comparison at the middle and low latitude regions

In this Section, we will compare the middle and low latitude thermosphere and ionosphere of the OIM-FAC simulation to the Weimer-POT and AMIE-POT simulations to assess the general differences amongst them. The zonal mean wind at 350 km is illustrated in Figure 10 over geographic latitude and DOY (meridional/zonal wind is defined as northward/eastward positive). On the geomagnetically active DOY 149, the Joule heating rate from the Weimer simulation is up to twice as large as compared to the other two cases (Figure 9), and therefore the neutral wind is more equatorward and westward for the Weimer-POT case, especially in the northern hemisphere. In the southern middle latitude region the zonal mean zonal wind of the OIM-FAC simulation tends to be more eastward compared to the other two simulations associated with the smaller southern hemisphere Joule heating rate of the OIM-FAC simulation.

Due to the sudden increase in the high latitude Joule heating input there are signatures of traveling atmospheric disturbances (TAD) with a phase speed of approximately 590 m/s in the meridional wind as derived from the slope of the disturbance traveling from the polar region toward the equator over time. These signatures are most pronounced in the AMIE-POT simulation, but also present in the OIM-FAC simulation with smaller wind amplitudes. In the Weimer-POT simulation, the TAD signatures are broader and the timing does not always agree with that from the AMIE-POT simulation.

Associated with the increased high latitude energy input into the ionosphere-thermosphere system in the Weimer-POT case, there is an approximately 20% larger zonal mean neutral density at 350 km at middle and low latitudes in the Weimer-POT case compared

to the AMIE-POT and the OIM-FAC simulations (Figure 11). The zonal mean neutral temperature at the geographic equator at 350 km (not depicted) is approximately by 7% larger in the Weimer-POT simulation compared to the AMIE-POT and OIM-FAC simulations, indicating that part of the neutral density increase is due to thermospheric expansion.

To compare absolute density magnitudes, we use derived densities from the Challenging Minisatellite Payload (CHAMP) and Gravity Recovery and Climate Experiment (GRACE)-B accelerometer data scaled to 400 km (Sutton, 2018) using the Mass-Spectrometer-Incoherent-Scatter (MSIS) model (Picone et al., 2002). The neutral density variations at approximately 7 local time (LT) and 16 LT are illustrated in Figure 12. For all three simulations the neutral density at 400 km during the quiescent DOY 148 is up to approximately 40-50% larger than the one derived from CHAMP and GRACE-B data at 7 LT and 16 LT, respectively. During the geomagnetically active DOY 149 and 150, the comparison is mixed. At 7 LT the neutral density from the Weimer-POT simulation tends to be larger than the one from CHAMP data; however at 16 LT the Weimer simulation captures the neutral density peak magnitudes around DOY 149.7 and 150.45. The AMIE-POT and the OIM-FAC simulations both underestimate the neutral density peaks at 16 LT, but the background magnitudes are comparable to the GRACE-B values. At 7 LT the AMIE-POT and OIM-FAC cases, but not the Weimer-POT case, capture better the interhemispheric differences and the general magnitude of the neutral density on DOY 149 and 150. Note that for the simulation results we do not consider the satellite orbits but include all longitudes for the specific local time, which is justified since we are not conducting a detailed model-data comparison but rather focus on the main differences among the three sets of simulations.

The magnetic-zonal mean peak electron density of the F2-layer (NmF2) is shown in Figure 13. All the simulations tend to have larger NmF2 peak values in the southern (winter) equatorial ionization anomaly (EIA) region compared to the northern (summer) EIA region. On DOY 149 the low latitude NmF2 of the Weimer simulation is larger than that for the AMIE-POT and OIM-FAC simulations, most likely associated with the larger daytime vertical equatorial drift during that time period in the Weimer simulation (Figure 15). Overall, the NmF2 from the OIM-FAC is smaller than that in the other two cases, which might be associated with the lower daytime vertical drift.

The increased mid-latitude NmF2 around $\lambda_q = -35^o$ to -45^o at DOY 149.4 is most pronounced in the Weimer-POT simulation and correlates with the enhanced equatorward neutral wind (Figure 10), which is indicative of neutral wind pushing plasma up the field-lines into regions of reduced recombination. The correlation between equatorward winds and increased middle latitude NmF2 is only apparent in the southern and not in the northern hemisphere, particularly in the Weimer-POT and AMIE-POT simulations and less pronounced in the OIM-FAC simulation. The zonal mean equatorward wind magnitude at middle latitude during geomagnetically disturbed times does not have a significant interhemispheric difference (e.g., Fuller-Rowell et al., 1996) to explain the interhemispheric difference in the middle latitude NmF2 (Figure 10). It should be pointed out that the zonal mean NmF2, in comparison with the zonal mean wind, is dominated by the daytime values which are several orders of magnitudes larger than night-time values.

It was shown that during solstice conditions the ionospheric storm time effects are negative in the summer and positive in the winter mid-latitude region (e.g., Fuller-Rowell et al., 1994; Araujo-Pradere et al., 2006; Stankov et al., 2010). Note that we focus on the zonal mean NmF2 in Figure 13, called the DC shift by Rodger et al. (1989) and not the local time variation. The positive and negative zonal mean NmF2 changes are associated with the summer-to-winter meridional circulation which enhances the [O]/[N_2] ratio in the winter hemisphere and during storm times the seasonal poleward wind in the winter hemisphere restrains the [O]/[N_2] ratio changes to the winter middle latitude region (e.g., Fuller-Rowell et al., 1996). This suggests that in the simulation in the northern middle latitude region the negative storm effects are compensated by the positive effect of the equatorward wind. Further examinations would be necessary which are beyond the scope of this study.

The differences in the Joule heating rate and their effect on the neutral dynamics are reflected in the zonal mean [O]/[N_2] ratio at 180 km illustrated in the Figure 14. On DOY 148, the [O]/[N_2] ratio exhibits normal solstice variation with larger ratios in the winter hemisphere than in the summer hemisphere (e.g., Luan et al., 2017). The southern high latitude [O]/[N_2] ratio (poleward of approximately $\lambda_q = -60^o$) of the AMIE-POT and Weimer-POT simulations is reduced compared to the OIM-FAC simulation, which is associated with the larger Joule heating rate enhancing the upward transport of [N_2] and reducing the [O]/[N_2] ratio in the former simulations. In the southern mid-

dle latitude region (approximately between $\lambda_q = -30$ to -45^o), the [O]/[N_2] ratio in the Weimer-POT and AMIE-POT simulations is increased, associated with the enhanced meridional mean circulation and atomic oxygen transport due to the increased Joule heating (see Figures 9 and 10). The compositional changes contribute to the comparatively larger NmF2 in the southern mid-latitude region in the AMIE-POT and WEIMER-POT simulations compared to the OIM-FAC simulation, which has weaker meridional mean circulation and a lower [O]/[N_2] ratio in that region.

The low latitude NmF2 also depends on the daytime equatorial vertical drift. In Figure 15 (left panels) the vertical ExB drift at the magnetic equator is presented over local time and DOY, and NmF2 (right panels) in the southern crest of the EIA at magnetic latitude $\lambda_q = -10^o$. The black dashed line indicates the solar local time variation of a point for geographic longitude $\phi_g = 0^o$ at the magnetic equator.

Overall, the vertical drift variations are similar for the three simulations, but there are also persistent differences. The OIM-FAC equatorial vertical drift in the daytime is lower than the drifts in the other two simulations, and it tends to have larger pre-dawn upward drift (4-6 LT). The occurrence time of the pre-dawn drift in all three simulations is similar. The temporal variability of the equatorial vertical drift is larger in the AMIE-POT and OIM-FAC simulations than in the WEIMER-POT simulation. The morning drift (4-8 LT) of all simulations has the tendency to be weakly upward or even downward, except for DOY 149, for longitudes close to $\phi_g = 0^o$.

The afternoon NmF2 correlates well with the morning vertical drift in the Weimer-POT simulation. At DOY 149.5 the morning drift is strongly upward between 6-8 LT and several hours afterwards the afternoon NmF2 is large. Around DOY 149.75 in the Weimer-POT simulation, the drift is downward between 6-12 LT and NmF2 is significantly reduced at the same geographic longitude for the rest of the daylit hours, compared with other days. This strong reduction in NmF2 does not occur in the AMIE-POT and OIM-FAC simulations. Overall, the result suggests that part of the lower afternoon NmF2 value in the OIM-FAC simulation is caused by the lower daytime equatorial vertical ExB drift compared to the other two simulations.

A more detailed picture of the diurnal variations of the equatorial vertical ExB drift at different longitudes is given in Figure 16. JULIA observations from the Jicamarca observatory are added by the green dots in Figure 16 a. The approximate nighttime is in-

dicated by the gray shaded area (18-6 LT). On the quiet DOY 148 the daytime vertical drift observations and the simulations agree well, except that the OIM-FAC drifts are less positive or more negative in the pre-noon hours. During the geomagnetically disturbed period, the daytime vertical drift of the OIM-FAC simulation tends to be smaller than for the other two cases. The agreement between the simulated vertical drift of the different cases varies with longitude, and in general the daytime drift of the OIM-FAC case is smaller, while the vertical drift of the AMIE-POT and Weimer-POT simulations agree well with each other. At $\phi_g = -76^o$ all three simulations show reasonable agreement with the JULIA drifts during day time.

The nighttime vertical drift of the OIM-FAC simulation is in general more variable than for the other two cases. For the OIM-FAC case, the electric field is solved for at high latitudes and not prescribed as in the Weimer-POT and AMIE-POT simulations; therefore the equatorial vertical drift is sensitive to the details about the high latitude conductance and field-line current distribution, which determine the electric field.

The total electron content (TEC) of the three simulations is compared to GPS TEC in Figure 17 for DOY 149 at 12 UT (DOY 149.5). As seen in the previous diagnostics the plasma density has the largest magnitude in the Weimer-POT simulation. For the OIM-FAC simulation, the EIA signature is more confined to the low latitude region but the magnitude is comparable to the AMIE-POT simulation. Overall, the TEC variations are similar among the 3 different simulations. The largest difference is at southern mid-latitudes, where the AMIE-POT and OIM-FAC simulations have a secondary latitudinal peak around geographic latitude $\lambda = -45^o$, but the Weimer simulation has a secondary latitudinal peak close to $\lambda = -30^o$. Further diagnostics indicates that neutral composition plays some role in the different peak location in the Weimer-POT simulation. In the $\lambda = -45^o$ region the N_2 mass mixing ratio in the Weimer simulation is approximately 50% larger than that in the other two cases, contributing to increased recombination in the lower F-region.

6 Summary and Conclusions

In this study, we present initial results from the TIEGCM with prescribed high latitude FAC based on the AMPERE data. In order to solve for asymmetric electric potential, we introduce a new approach by first, solving for the electric potential due to the

wind dynamo with prescribed high latitude FAC, then determine the residual FAC in each hemisphere, and use this residual FAC to determine a correction potential in the northern and southern polar regions, and in a final step add the potentials together. The wind dynamo has an influence on the high latitude electric potential, in contrast to approaches that specify the potential, like the Weimer-POT or AMIE-POT cases. The contribution of wind-driven ionospheric current to the FAC is on the order of 10% of the total FAC, usually in opposite direction of the prescribed FAC. In contrast, the polar electric potential is not affected by the wind dynamo in techniques that specify the high latitude electric potential, but the FAC is affected by the wind dynamo in such techniques.

Specifying the FAC versus an electric potential at high latitude describes the MI coupling as a pure current generator versus a voltage generator, respectively. Both are idealized ways to describe the magnetosphere-ionosphere coupling since ionospheric conductivities and the dynamo impose restrictions on the relation between electric fields and FAC, and the magnetospheric plasma pressure and plasma acceleration also constrain the FAC flowing into and out of the ionosphere. Specifying an electric potential or FAC does in general not satisfy the ionospheric and magnetospheric constraints simultaneously.

As with any new approach, it is important to compare to widely used and accepted methods. Therefore, we simulate the 28-30 May 2010 time period using the TIEGCM with specified high latitude Weimer electric potential, AMIE electric potential and auroral particle precipitation, and prescribed FAC. Since the assimilative AMIE procedure ingests various observations to get optimal specification of the electric potential and auroral particle precipitation, we consider, in general, the AMIE patterns and the associated simulation as closest to reality overall, although the AMPERE inputs should be most representative of the actual FAC.

We did not tune any simulation, but adjusted the default auroral parametrization in the TIEGCM for the prescribed FAC since the auroral oval parametrization in the TIEGCM is adjusted to fit to the Weimer electric potential, which is not necessarily suitable for the observed FAC distribution. We modified the default aurora parametrization by increasing the aurora oval width and reducing the energy flux, decreasing the aurora circle offset toward midnight, and increasing the default offset toward dawn.

Comparing the three simulations, we find that the new approach with specified high latitude FAC produces the spatial and temporal variations in the ionosphere and thermosphere during the 28-30 May 2010 time period with the same general characteristics as the other two techniques. The employed specified high latitude OIM-FAC was weaker, especially in the southern hemisphere, compared to the AMPERE-FAC data product and the AMIE procedure. This reduction is probably associated with the processing of the magnetic perturbations to derive smooth FAC distributions (Shi et al., 2020b). Since the focus of the current study is on the introduction of the new method, we did not attempt to improve the agreement between the three FAC distributions.

The temporal variation of the hemispherically integrated Joule heating rate compares favorably to the AMIE driven simulation. The Joule heating rates from the AMIE-POT and OIM-FAC simulations tend to be smaller than that from the Weimer simulation, which is associated with the magnitude difference in the polar potential drop between these simulations.

Due to the difference in the Joule heating rate between the Weimer-POT and the other AMIE-POT and OIM-FAC simulations, the zonal mean neutral wind is more equatorward and westward in the Weimer-POT simulation, leading to reduced high latitude $[O]/[N_2]$ ratio, especially in the southern hemisphere. The OIM-FAC simulation behaves similarly to the AMIE-POT simulation in terms of the neutral dynamics and neutral density magnitude and variations. Comparison with neutral density derived from CHAMP and GRACE-B accelerometer data indicates that the Weimer-POT simulation captures the storm-time peak neutral density magnitude on DOY 149 at 16 LT well, while the neutral density from AMIE-POT and OIM-FAC simulations tends to be low at this local time. However, at 7 LT the Weimer-POT simulation overestimates the neutral density while AMIE-POT and OIM-FAC simulated magnitudes and especially the interhemispheric differences agree better with the satellite observations.

The OIM-FAC simulated ionosphere is in general consistent with the Weimer-POT and AMIE-POT simulations. However, there are some systematic differences. In general, the low latitude NmF2 from the OIM-FAC simulation is smaller than that from the other two simulations. A potential cause is the smaller daytime upward equatorial drift. The spatial distribution of the NmF2 is similar in the AMIE-POT and OIM-FAC simulations. Using prescribed FAC compared to prescribed electric potential increases the

variability of the night-time equatorial electric field since the electric potential depends on the auroral conductances in the prescribed FAC case.

In this first study, we demonstrate that using prescribed FAC at high latitude in the TIEGCM compares well with the simulation driven by AMIE electric potential and auroral particle precipitation. The new approach can be used to include observed high latitude FAC in GCMs to study their effects on the TI system. In addition, the new approach might be useful in coupling magnetospheric models to thermosphere-ionosphere models via FACs as they are direct output of MHD models.

Future work includes the careful examination of the magnitude of the FAC distribution to ensure data processing does not introduce unintended effects. In the case of prescribed high latitude FAC, the mismatch between FAC and auroral precipitation distributions can lead to unreasonable electric potential solutions, which affect also the equatorial electric field variations. This highlights the importance of having better specifications of the auroral particle precipitation, even on large scales, which are consistent with the FAC (e.g., Marsal et al., 2012; Zhu et al., 2020). Overall, more events need to be examined with the new approach to gain more experience and solidify our initial findings.

Acknowledgments

A.M., A.R. and G.L were supported by AFOSR through award FA9559-17-1-0248, the Living with a Star program under NASA grant 80NSSC17K071, and the Heliophysics Supporting Research program under NASA grant NNX17AI39G. DJK and YS were supported by AFOSR through MURI award FA9559-16-1-0364 and by AFOSR Award Award No: FA9550-17-1-0258. The model simulation associated with this publication is available at the NCAR Digital Access Service Hub (DASH) https://doi.org/10.5065/77xn-3n58. We thank the AMPERE team and the AMPERE Science Center for providing the Iridium derived data products (http://ampere.jhuapl.edu/dataget/index.html). We acknowledge the use of NASA/GSFC's Space Physics Data Facility's OMNIWeb service, and OMNI data (https://omniweb.gsfc.nasa.gov/form/omni_min.html). We acknowledge use of JULIA radar data from the Jicamarca Radio Observatory, a facility of the Instituto Geofísico del Perú operated with support from the NSF through Cornell University (http://jro-db.igp.gob.pe/madrigal/). GPS TEC data products (http://millstonehill.haystack.mit.edu/) and access through the Madrigal distributed data system are provided to the commu-

nity by the Massachusetts Institute of Technology under support from US National Science Foundation grant AGS-1242204. Data for the TEC processing is provided from the following organizations: UNAVCO, Scripps Orbit and Permanent Array Center, Institut Geographique National, France, International GNSS Service, The Crustal Dynamics Data Information System (CDDIS), National Geodetic Survey, Instituto Brasileiro de Geografia e Estatstica, RAMSAC CORS of Instituto Geográfico Nacional de la República Argentina, Arecibo Observatory, Low-Latitude Ionospheric Sensor Network (LISN), Topcon Positioning Systems, Inc., Canadian High Arctic Ionospheric Network, Institute of Geology and Geophysics, Chinese Academy of Sciences, China Meteorology Administration, Centro di Ricerche Sismologiche, Système d'Observation du Niveau des Eaux Littorales (SONEL), RENAG : REseau NAtional GPS permanent, GeoNet - the official source of geological hazard information for New Zealand, GNSS Reference Networks, Finnish Meteorological Institute, SWEPOS - Sweden, Hartebeesthoek Radio Astronomy Observatory, Crustal Dynamics Data Information System (CDDIS), Astronomical Institute of the University of Bern, TrigNet Web Application, South Africa, Australian Space Weather Services, RETE INTEGRATA NAZIONALE GPS, Estonian Land Board, and Virginia Tech Center for Space Science and Engineering Research. We are grateful to Eric Sutton for providing the neutral density data derived from CHAMP and GRACE (doi:10.5281/zenodo.1068523). The authors would like to thank Wenbin Wang for valuable comments on an earlier draft. We would like to acknowledge high-performance computing support from Cheyenne (doi:10.5065/D6RX99HX) provided by NCAR's Computational and Information Systems Laboratory, sponsored by the National Science Foundation. This material is based upon work supported by the National Center for Atmospheric Research, which is a major facility sponsored by the National Science Foundation under Cooperative Agreement No. 1852977.

References

Anderson, B., Korth, H., Waters, C., Green, D., Merkin, V., Barnes, R., & Dyrud, L. (2014). Development of large-scale Birkeland currents determined from the Active Magnetosphere and Planetary Electrodynamics Response Experiment. *Geophysical Research Letters*, *41*(9), 3017–3025. doi: 10.1002/2014GL059941

Anderson, B., Ohtani, S.-I., Korth, H., & Ukhorskiy, A. (2005). Storm time dawn-dusk asymmetry of the large-scale Birkeland currents. *Journal of Geophysical Research: Space Physics*, *110*(A12). doi: 10.1029/2005JA011246

Anderson, B., Takahashi, K., Kamei, T., Waters, C. L., & Toth, B. A. (2002). Birkeland current system key parameters derived from Iridium observations: Method and initial validation results. *Journal of Geophysical Research: Space Physics*, *107*(A6), SMP 11-1-SMP 11-13. doi: 10.1029/2001JA000080

Anderson, B., Takahashi, K., & Toth, B. A. (2000). Sensing global Birkeland currents with Iridium engineering magnetometer data. *Geophysical Research Letters*, *27*(24), 4045-4048. doi: 10.1029/2000GL000094

Araujo-Pradere, E., Fuller-Rowell, T., & Spencer, P. (2006). Consistent features of TEC changes during ionospheric storms. *Journal of Atmospheric and Solar-Terrestrial Physics*, *68*(16), 1834 - 1842. doi: https://doi.org/10.1016/j.jastp.2006.06.004

Berchem, J., Richard, R., Escoubet, C., Wing, S., & Pitout, F. (2016). Asymmetrical response of dayside ion precipitation to a large rotation of the IMF. *Journal of Geophysical Research: Space Physics*, *121*(1), 263–273.

Clausen, L. B. N., Baker, J. B. H., Ruohoniemi, J. M., Milan, S. E., & Anderson, B. J. (2012). Dynamics of the region 1 Birkeland current oval derived from the Active Magnetosphere and Planetary Electrodynamics Response Experiment (AMPERE). *Journal of Geophysical Research: Space Physics*, *117*(A6). doi: 10.1029/2012JA017666

Codrescu, M., Fuller-Rowell, T. J., & Foster, J. C. (1995). On the importance of E-field variability for Joule heating in the high-latitude thermosphere. *Geophysical Research Letters*, *22*(17), 2393 2396. doi: 10.1029/95GL01909

Cousins, E., Matsuo, T., & Richmond, A. D. (2013). SuperDARN assimilative mapping. *Journal of Geophysical Research*, *118*(12), 7954–7962. doi: 10.1002/2013JA019321

Cousins, E., Matsuo, T., & Richmond, A. D. (2015). Mapping high-latitude ionospheric electrodynamics with SuperDARN and AMPERE. *Journal of Geophysical Research: Space Physics*, *120*(7), 5854-5870. doi: 10.1002/2014JA020463

Cousins, E., Matsuo, T., Richmond, A. D., & Anderson, B. J. (2015). Dominant modes of variability in large-scale Birkeland currents. *Journal of Geophysical Research: Space Physics*, *120*(8), 6722-6735. doi: 10.1002/2014JA020462

Coxon, J. C., Milan, S. E., Carter, J. A., Clausen, L. B. N., Anderson, B. J., & Korth, H. (2016). Seasonal and diurnal variations in AMPERE observations of

the Birkeland currents compared to modeled results. *Journal of Geophysical Research Space Physics*, *121*, 4027-4040. doi: doi:10.1002/2015JA022050

Dickinson, R. E., Ridley, E., & Roble, R. (1984). Thermospheric general circulation with coupled dynamics and composition. *Journal of the Atmospheric Sciences*, *41*(2), 205–219.

Emery, B., Roble, R., Ridley, E., Richmond, A., Knipp, D., Crowley, G., ... Maeda, S. (2012). *Parameterization of the ion convection and the auroral oval in the NCAR Thermospheric General Circulation Models* (Tech. Rep.). National Center for Atmospheric Research, Boulder CO, USA. doi: 10.5065/D6N29TXZ

Förster, M., & Haaland, S. (2015). Interhemispheric differences in ionospheric convection: Cluster EDI observations revisited. *Journal of Geophysical Research: Space Physics*, *120*(7), 5805–5823.

Fujii, R., Iijima, T., Potemra, T. A., & Sugiura, M. (1981). Seasonal dependence of large-scale Birkeland currents. *Geophysical Research Letters*, *8*(10), 1103–1106.

Fukushima, N. (1979). Electric potential difference between conjugate points in middle latitudes caused by asymmetric dynamo in the ionosphere. *Journal of Geomagnetism and Geoelectricity*, *31*, 401–409.

Fuller-Rowell, T. J., Codrescu, M. V., Moffett, R. J., & Quegan, S. (1994). Response of the thermosphere and ionosphere to geomagnetic storms. *Journal of Geophysical Research*, *99*(A3), 3893–3914. doi: 10.1029/93JA02015

Fuller-Rowell, T. J., Codrescu, M. V., Rishbeth, H., Moffett, R. J., & Quegan, S. (1996). On the seasonal response of the thermosphere and ionosphere to geomagnetic storms. *Journal of Geophysical Research: Space Physics*, *101*(A2), 2343-2353. doi: 10.1029/95JA01614

Fuller-Rowell, T. J., & Evans, D. S. (1987). Height-integrated Pedersen and Hall conductivity patterns inferred from the TIROS-NOAA satellite data. *Journal of Geophysical Research: Space Physics*, *92*(A7), 7606-7618. doi: 10.1029/JA092iA07p07606

Heelis, R. A., Lowell, J. K., & Spiro, R. W. (1982). A model of the high-latitude ionospheric convection pattern. *Journal of Geophysical Research*, *87*(A8), 6339–6345. doi: 10.1029/JA087iA08p06339

Heelis, R. A., & Maute, A. (2020). Challenges to understanding the Earth's iono-

sphere and thermosphere. *Journal of Geophysical Research*, *125*. doi: 10.1029/2019JA027497

Korth, H., Anderson, B. J., Frey, H. U., & Waters, C. L. (2005). High-latitude electromagnetic and particle energy flux during an event with sustained strongly northward IMF. *Annales Geophysicae*, *23*(4), 1295–1310. Retrieved from `https://www.ann-geophys.net/23/1295/2005/` doi: 10.5194/angeo-23-1295-2005

Lei, J., Zhu, Q., Wang, W., Burns, A. G., Zhao, B., Luan, X., ... Dou, X. (2015). Response of the topside and bottomside ionosphere at low and middle latitudes to the October 2003 superstorms. *Journal of Geophysical Research: Space Physics*, *120*(8), 6974–6986. doi: 10.1002/2015JA021310

Lu, G. (2017). Large scale high-latitude ionospheric electrodynamic fields and currents. *Space Science Reviews*, *206*(1), 431–450. doi: 10.1007/s11214-016-0269-9

Lu, G., Hagan, M. E., Häusler, K., Doornbos, E., Bruinsma, S., Anderson, B. J., & Korth, H. (2014). Global ionospheric and thermospheric response to the 5 April 2010 geomagnetic storm: An integrated data-model investigation. *Journal of Geophysical Research: Space Physics*, *119*(12), 10,358-10,375. doi: 10.1002/2014JA020555

Lu, G., Richmond, A., Emery, B., & Roble, R. (1995). Magnetosphere-ionosphere-thermosphere coupling: Effect of neutral winds on energy transfer and field-aligned current. *Journal of Geophysical Research: Space Physics*, *100*(A10), 19643–19659.

Lu, G., Richmond, A. D., Roble, R. G., & Emery, B. A. (2001). Coexistence of ionospheric positive and negative storm phases under northern winter conditions: A case study. *Journal of Geophysical Research*, *106*(A11), 24493–24504. doi: 10.1029/2001JA000003

Luan, X., Wang, W., Burns, A., & Dou, X. (2017). Solar cycle variations of thermospheric O/N2 longitudinal pattern from TIMED/GUVI. *Journal of Geophysical Research: Space Physics*, *122*(2), 2605-2618. doi: 10.1002/2016JA023696

Lühr, H., Kervalishvili, G., Michaelis, I., Rauberg, J., Ritter, P., Park, J., ... Brauer, P. (2015). The interhemispheric and F region dynamo currents revisited with the Swarm constellation. *Geophysical Research Letters*, *42*(9),

3069–3075. doi: 10.1002/2015GL063662

Lukianova, R., Hanuise, C., & Christiansen, F. (2008). Asymmetric distribution of the ionospheric electric potential in the opposite hemispheres as inferred from the SuperDARN observations and FAC-based convection model. *Journal of Atmospheric and Solar-Terrestrial Physics*, *70*(18), 2324–2335.

Marsal, S. (2015). Conductivities consistent with Birkeland currents in the AMPERE-driven TIE-GCM. *Journal of Geophysical Research: Space Physics*, *120*(9), 8045-8065. doi: 10.1002/2015JA021385

Marsal, S., Richmond, A., Maute, A., & Anderson, B. (2012). Forcing the TIEGCM model with Birkeland currents from the Active Magnetosphere and Planetary Electrodynamics Response Experiment. *Journal of Geophysical Research*, *117*(A6).

Matsuo, T., Knipp, D. J., Richmond, A. D., Kilcommons, L., & Anderson, B. J. (2015). Inverse procedure for high-latitude ionospheric electrodynamics: Analysis of satellite-borne magnetometer data. *Journal of Geophysical Research: Space Physics*, *120*(6), 5241-5251. doi: 10.1002/2014JA020565

Nishimura, T., Deng, Y., Lyons, L. R., McGranaghan, R. M., & Zettergren, M. D. (2020). Multi-scale dynamics in the high-latitude ionosphere. In *Solar/heliosphere 3: Advances in ionospheric research.* Wiley Online Library.

Park, J., Lühr, H., & Min, K. W. (2011). Climatology of the inter-hemispheric field-aligned current system in the equatorial ionosphere as observed by CHAMP. *Ann. Geophysicae*, *29*, 573-582. doi: 10.5194/angeo-29-573-2011

Pettigrew, E., Shepherd, S., & Ruohoniemi, J. (2010). Climatological patterns of high-latitude convection in the northern and southern hemispheres: Dipole tilt dependencies and interhemispheric comparisons. *Journal of Geophysical Research: Space Physics*, *115*(A7).

Picone, J. M., Hedin, A. E., Drob, D. P., & Aikin, A. C. (2002). NRLMSISE-00 empirical model of the atmosphere: Statistical comparisons and scientific issues. *Journal of Geophysical Research: Space Physics*, *107*(A12). doi: 10.1029/2002JA009430

Qian, L., Burns, A. G., Emery, B. A., Foster, B., Lu, G., Maute, A., ... Wang, W. (2014). The NCAR TIE-GCM: A community model of the coupled thermosphere/ionosphere system. *Modeling the Ionosphere-Thermosphere System,*

Geophys. Monogr. Ser, *201*, 73–83.

Raeder, J., Wang, Y., & Fuller-Rowell, T. J. (2001). Geomagnetic storm simulation with a coupled magnetosphere-ionosphere-thermosphere model. *Washington DC American Geophysical Union Geophysical Monograph Series*, *125*, 377–384.

Richards, P., Fennelly, J., & Torr, D. (1994). EUVAC: A solar EUV flux model for aeronomic calculations. *Journal of Geophysical Research*, *99*, 8981–1992.

Richmond, A. (1992). Assimilative mapping of ionospheric electrodynamics. *Advances in Space Research*, *12*(6), 59–68.

Richmond, A. (1995). Ionospheric Electrodynamics Using Magnetic Apex Coordinates. *Journal of Geomagnetism and Geoelectricity*, *47*(2), 191-212.

Richmond, A., & Maute, A. (2013). Ionospheric electrodynamics modeling. In R. S. J.D. Huba & G. Khazanov (Eds.), *Modeling the ionosphere-thermosphere* (Vol. 201, pp. (also published online in 2014 by John Wiley & Sons, Ltd, Chichester, UK. doi:10.1002/9781118704417.ch6)). AGU Geophysical Monograph Series. doi: 10.1029/2012GM001331

Richmond, A., & Maute, A. (2014). Ionospheric electrodynamics modeling. *Modeling the Ionosphere-Thermosphere System*, 57–71. doi: 10.1002/9781118704417.ch6

Richmond, A., Ridley, E. C., & Roble, R. G. (1992). A thermosphere/ionosphere general circulation model with coupled electrodynamics. *Geophysical Research Letters*, *19*(6), 601–604. doi: 10.1029/92GL00401

Roble, R., & Ridley, E. (1987). An auroral model for the NCAR thermospheric general circulation model (TGCM). *Annales Geophysicae*, *5A*, 369-382.

Roble, R., Ridley, E., & Richmond, A. (1988). A coupled thermosphere / ionosphere general circulation model. *Geophys. Res. Letters*, *15*, 1325–1328.

Rodger, A. S., Wrenn, G., & Rishbeth, H. (1989). Geomagnetic storms in the antarctic F-region. II. Physical interpretation. *Journal of Atmospheric and Terrestrial Physics*, *51*(11-12), 851–866. doi: 10.1016/0021-9169(89)90002-0

Shi, Y., Knipp, D., Matsuo, T., Kilcommons, L., & Anderson, B. (2020a). Event studies of high-latitude field-aligned currents (FACs) with inverse and assimilative analysis of AMPERE magnetometer data. *Journal of Geophysical Research: Space Physics*.

Shi, Y., Knipp, D., Matsuo, T., Kilcommons, L., & Anderson, B. (2020b). Modes of field-aligned currents (FACs) variability and their hemispheric asymmetry revealed by inverse and assimilative analysis of Iridium magnetometer data. *Journal of Geophysical Research: Space Physics*.

Stankov, S., Stegen, K., & Warnant, R. (2010). Seasonal variations of storm-time TEC at European middle latitudes. *Advances in Space Research*, *46*(10), 1318 - 1325. doi: https://doi.org/10.1016/j.asr.2010.07.017

Sutton, E. K. (2018). A new method of physics-based data assimilation for the quiet and disturbed thermosphere. *Space Weather*, *16*(6), 736–753.

Tóth, G., Sokolov, I. V., Gombosi, T. I., Chesney, D. R., Clauer, C. R., De Zeeuw, D. L., ... Kóta, J. (2005). Space weather modeling framework: A new tool for the space science community. *Journal of Geophysical Research: Space Physics*, *110*(A12). doi: 10.1029/2005JA011126

Waters, C. L., Anderson, B. J., & Liou, K. (2001). Estimation of global field aligned currents using the Iridium system magnetometer data. *Geophysical Research Letters*, *28*(11), 2165-2168.

Weimer, D. R. (2005). Improved ionospheric electrodynamic models and application to calculating Joule heating rates. *Journal of Geophysical Research*, *110*(A5). doi: 10.1029/2004JA010884

Wilder, F. D., Crowley, G., Anderson, B. J., & Richmond, A. D. (2012). Intense dayside Joule heating during the 5 April 2010 geomagnetic storm recovery phase observed by AMIE and AMPERE. *Journal of Geophysical Research: Space Physics*, *117*(A5). doi: 10.1029/2011JA017262

Wiltberger, M. (2015). Review of global simulation studies of effect of ionospheric outflow on magnetosphere-ionosphere system dynamics. In *Magnetotails in the solar system* (Vol. 207, pp. 373–392).

Wiltberger, M., Wang, W., Burns, A., Solomon, S., Lyon, J., & Goodrich, C. (2004). Initial results from the coupled magnetosphere ionosphere thermosphere model: magnetospheric and ionospheric responses. *Journal of Atmospheric and Solar-Terrestrial Physics*, *66*(15), 1411 - 1423. doi: https://doi.org/10.1016/j.jastp.2004.03.026

Winglee, R., Chua, D., Brittnacher, M., Parks, G., & Lu, G. (2002). Global impact of ionospheric outflows on the dynamics of the magnetosphere and cross-polar

cap potential. *Journal of Geophysical Research: Space Physics*, *107*(A9), SMP–11.

Yang, J., Toffoletto, F., Lu, G., & Wiltberger, M. (2014). RCM-E and AMIE studies of the Harang reversal formation during a steady magnetospheric convection event. *Journal of Geophysical Research: Space Physics*, *119*(9), 7228-7242. doi: 10.1002/2014JA020207

Zhang, B., Sorathia, K. A., Lyon, J. G., Merkin, V. G., Garretson, J. S., & Wiltberger, M. (2019). GAMERA: A three-dimensional finite-volume MHD solver for non-orthogonal curvilinear geometries. *The Astrophysical Journal Supplement Series*, *244*(1), 20.

Zhang, X., Forbes, J. M., & Hagan, M. E. (2010a). Longitudinal variation of tides in the MLT region: 1. Tides driven by tropospheric net radiative heating. *Journal of Geophysical Research: Space Physics*, *115*(A6). doi: 10.1029/2009JA014897

Zhang, X., Forbes, J. M., & Hagan, M. E. (2010b). Longitudinal variation of tides in the MLT Region: 2. relative effects of solar radiative and latent heating. *Journal of Geophysical Research*, *115*(A6). doi: 10.1029/2009JA014898

Zhu, Q., Deng, Y., Richmond, A., Maute, A., Chen, Y.-J., Hairston, M., ... Mitchell, E. (2020). Impacts of binning methods on high-latitude electrodynamic forcing: static vs boundary-oriented binning methods. *Journal of Geophysical Research: Space Physics*, *125*(1). doi: 10.1029/2019JA027270

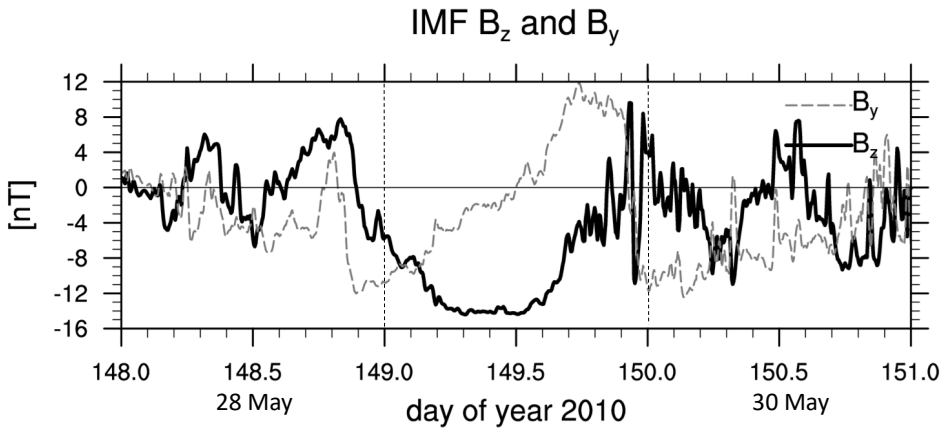

Figure 1. IMF B_y and B_z [nT] for 28-30 May 2010 based on NASA SPDF-OMNIweb data [`https://omniweb.gsfc.nasa.gov`].

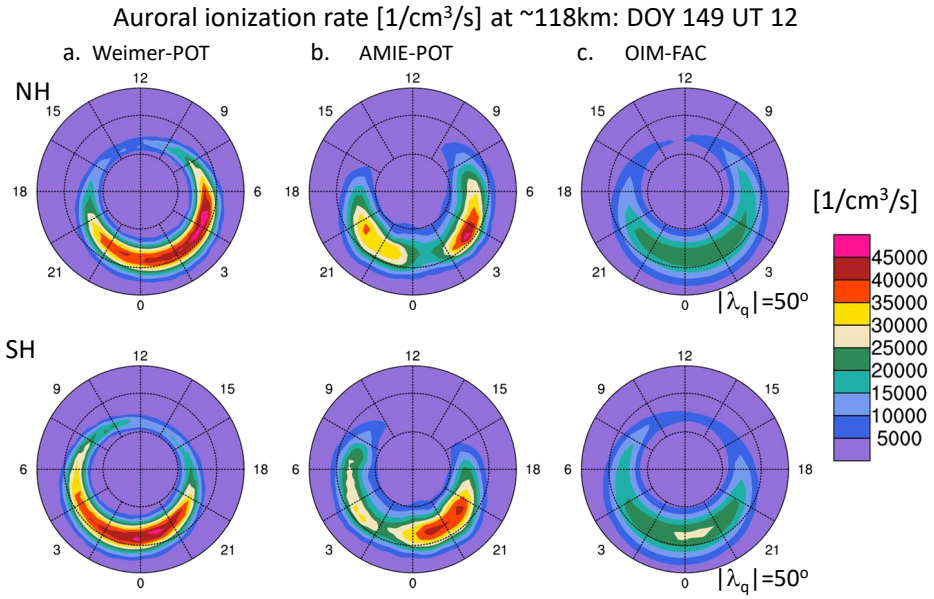

Figure 2. Auroral ionization rate $[\frac{1}{cm^3 s}]$ poleward of $\pm 50^o$ quasi dipole latitude for 29 May 2010 (DOY 149 UT 12) for a. Weimer-POT case, b. AMIE auroral precipitation, and c. OIM-FAC case for northern hemisphere (top) and southern hemisphere (bottom) with Weimer-POT case and OIM-FAC case using the TIEGCM default analytical aurora model but with different parametrization (see Supporting Information)(Roble & Ridley, 1987).

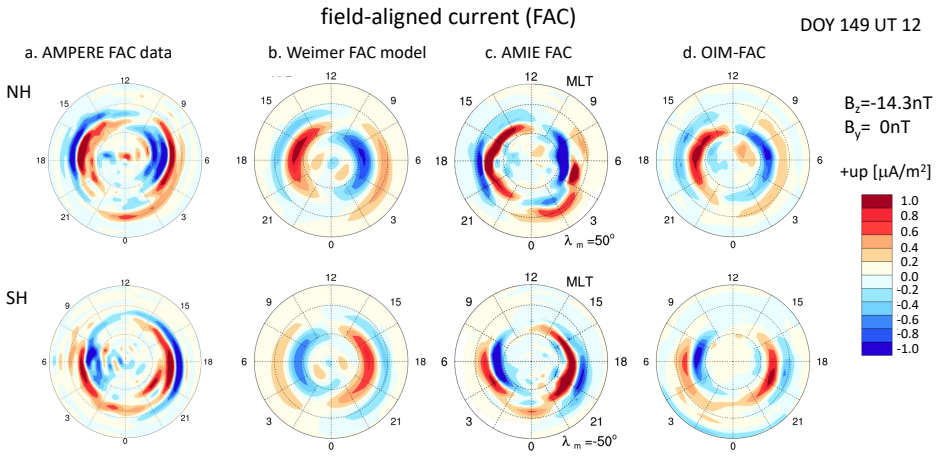

Figure 3. Field-aligned current [$\mu A/m^2$] (positive is upward) for 29 May 2010 (doy 149) at 12 UT plotted over magnetic local time (MLT) in northern hemisphere (NH, top panels) and southern hemisphere (SH, bottom panels) from different sources: a. AMPERE FAC data product [`http://ampere.jhuapl.edu/`], b. empirical Weimer FAC model (Weimer, 2005), c. FAC from AMIE procedure, and d. FAC using OI method. Note that these patterns are not based on TIEGCM simulations.

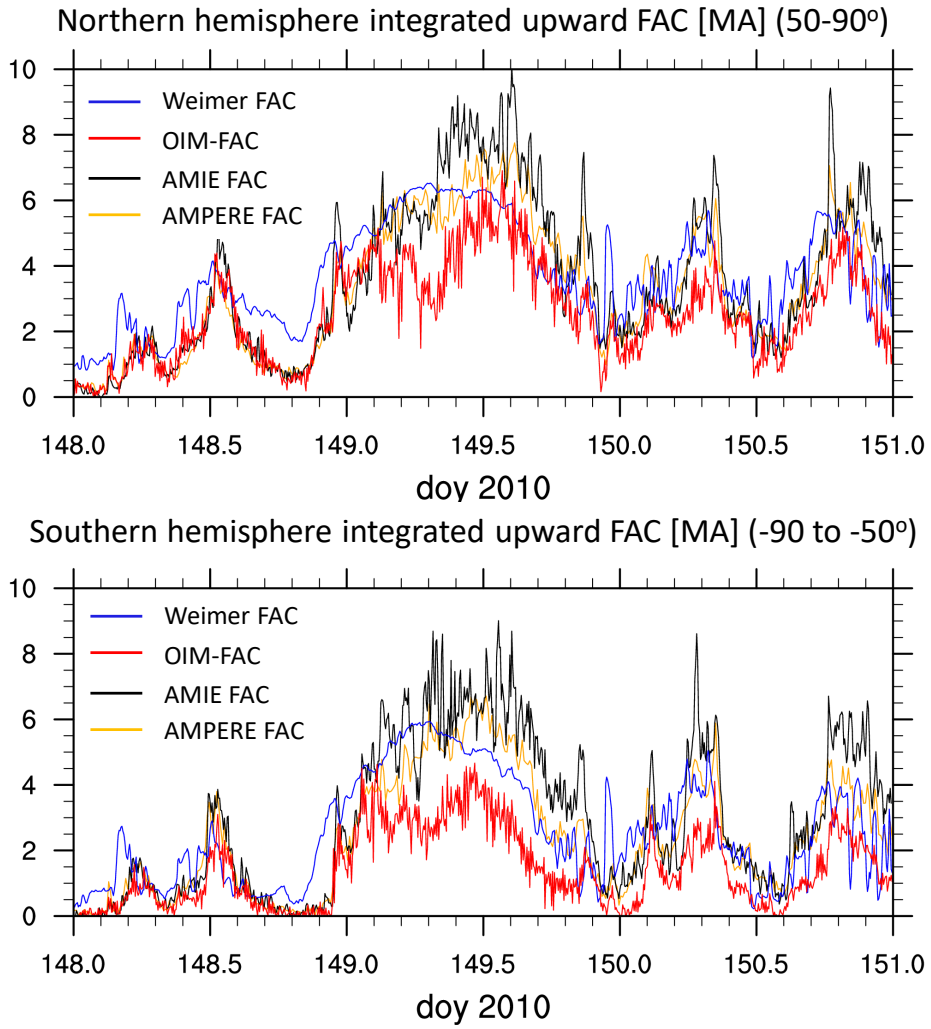

Figure 4. Hemispherically integrated upward field-aligned current [MA] poleward of $\lambda_q = 50^o$ in the northern hemisphere (NH, top panels) and southern hemisphere (SH, bottom panels) from different sources: AMPERE FAC data product `http://ampere.jhuapl.edu/` (orange lines), empirical Weimer FAC model (Weimer, 2005) (blue lines), FAC from AMIE procedure (black lines), and OIM-FAC (red lines).

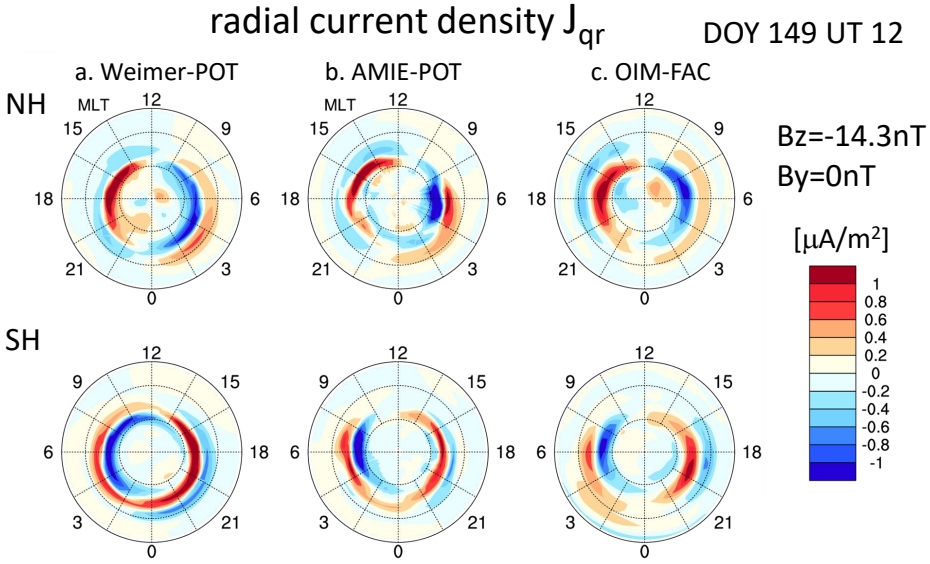

Figure 5. Radial current density J_{qr} $[\mu A/m^2]$ (positive is upward) for 29 May 2010 (doy 149) at 12 UT based on the TIEGCM simulations for a. Weimer-POT, b. AMIE-POT, and c. OIM-FAC cases for the northern hemisphere (NH, top panels) and southern hemisphere (SH, bottom panels) over MLT and magnetic latitude (perimeter latitude is $\pm 50^o$).

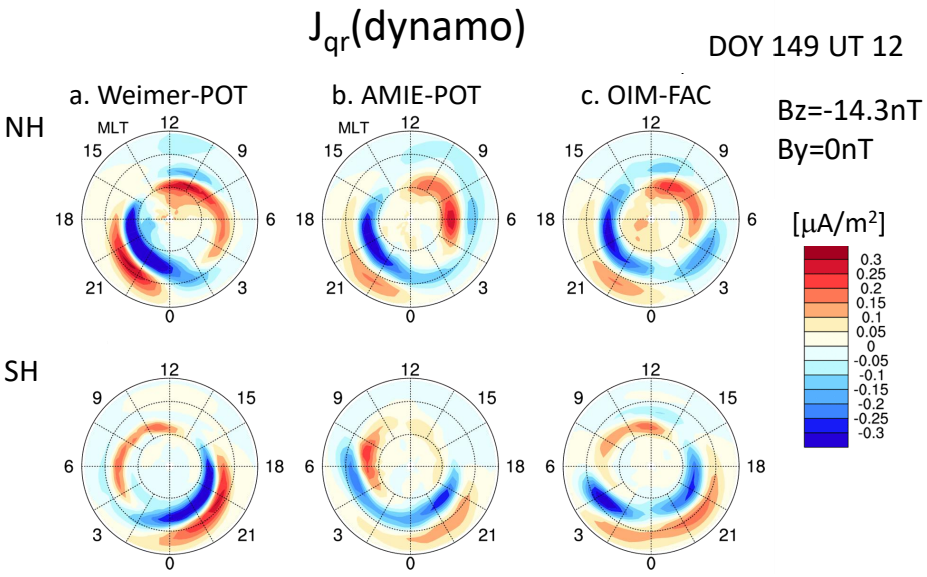

Figure 6. Radial current density J_{qr} $[\mu A/m^2]$ (positive is upward) for 29 May 2010 (day of year 149) at 12 UT due to the wind dynamo based on TIEGCM simulations for a. Weimer-POT, b. AMIE-POT, and c. OIM-FAC cases for the northern hemisphere (NH, top panels) and southern hemisphere (SH, bottom panels) over MLT and magnetic latitude (perimeter is $\pm 50^o$ magnetic latitude).

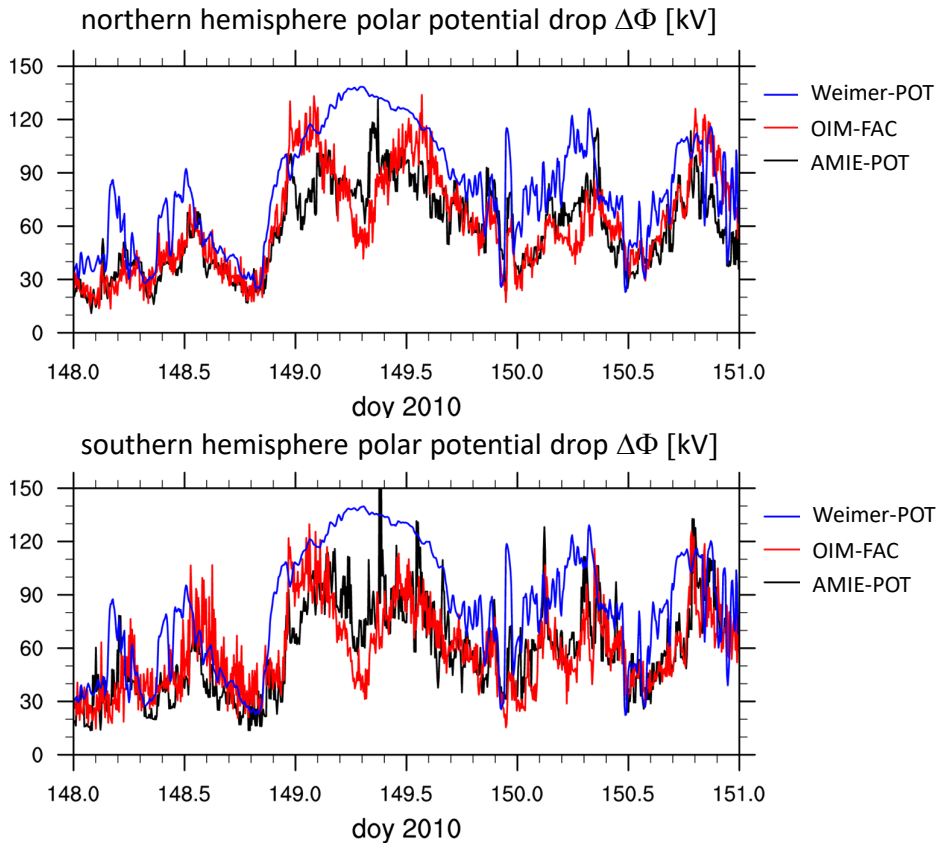

Figure 7. Polar potential drop [kV] poleward of $\pm 50^o$ magnetic latitude based on simulations for Weimer-POT (blue), AMIE-POT (black), and OIM-FAC (red) cases for northern hemisphere (top) and southern hemisphere (bottom)

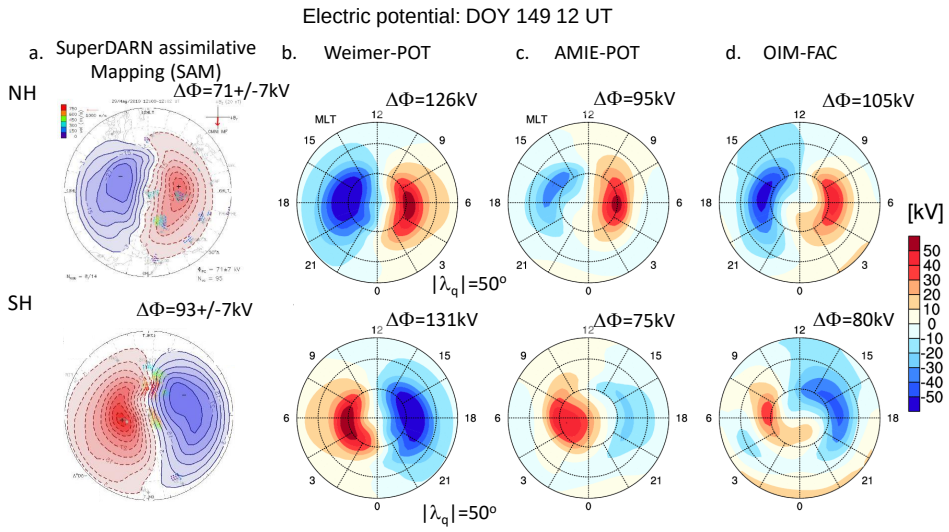

Figure 8. Electric potential [kV] poleward of $\pm 50^o$ magnetic latitude for 29 May 2010 (doy 149 UT 12) based on a. SuperDARN assimilative mapping (SAM) (Cousins et al., 2013) (2 min window) [VT.superdarn.org], and simulations b. Weimer-POT, c. AMIE-POT, and d. OIM-FAC cases for the northern hemisphere (top panels) and southern hemisphere (bottom panels)

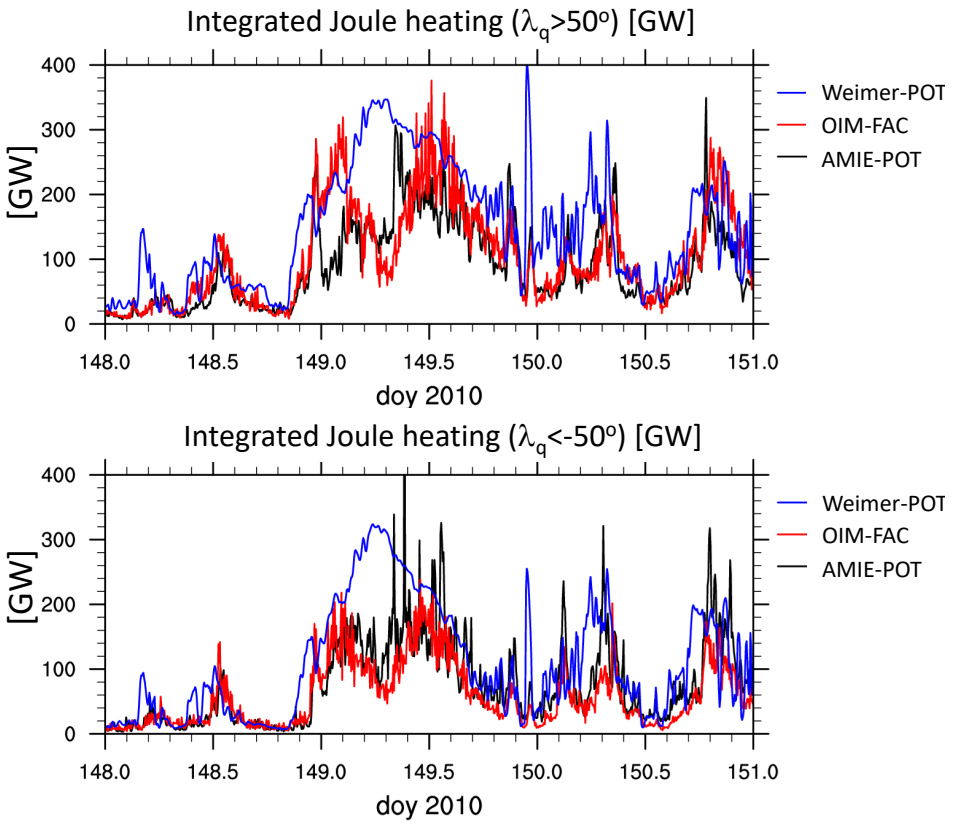

Figure 9. Hemispherically integrated Joule heating [GW] poleward of $\pm 50^o$ magnetic latitude based on simulations Weimer-POT (blue), AMIE-POT (black), and OIM-FAC (red) cases for the northern hemisphere (top) and southern hemisphere (bottom)

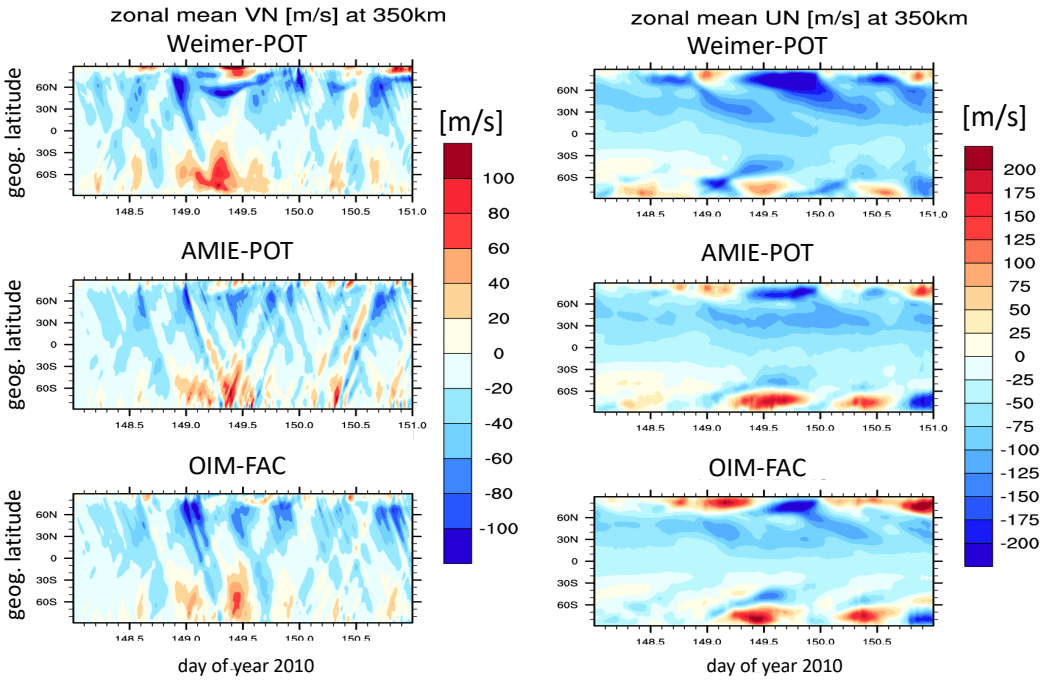

Figure 10. Zonal mean meridional (left panels) and zonal (right panels) neutral wind [m/s] at 350 km altitude over geographic latitude and day of year (DOY) 2010 for the simulations Weimer-POT (top), AMIE-POT (middle), and OIM-FAC (bottom).

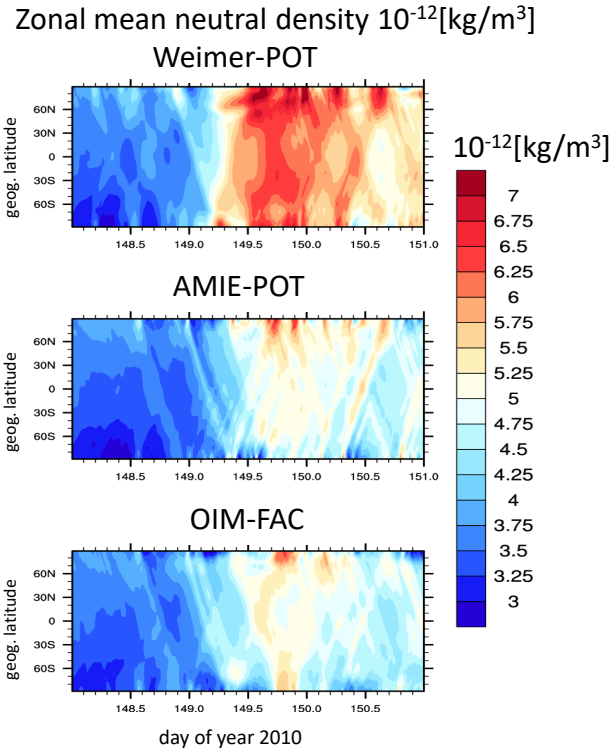

Figure 11. Zonal mean neutral density $10^{-12}[kg/m^3]$ at 350km over geographic latitude and day of year (DOY) 2010 for the simulations Weimer-POT (top), AMIE-POT (middle), and OIM-FAC (bottom).

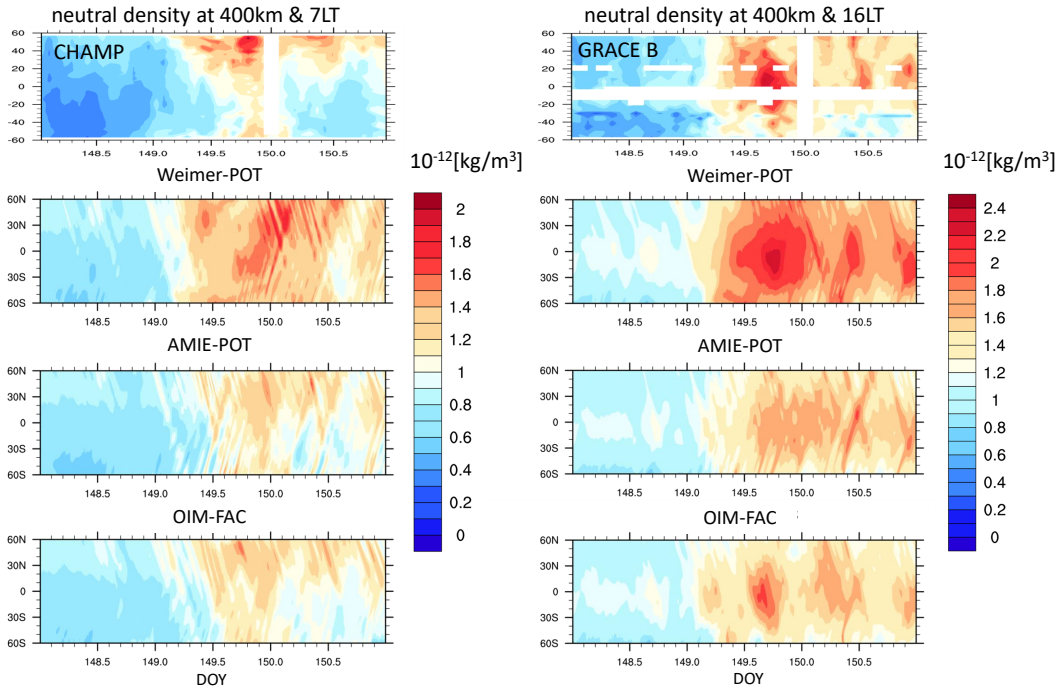

Figure 12. Neutral density $10^{-12}[kg/m^3]$ at 400km over geographic latitude and day of year (doy) 2010 at 7 LT (left panels) and 16 LT (right panels) based on neutral densities scaled to 400 km from CHAMP (top left panel) and GRACE-B (top right panel) and the simulations Weimer-POT (second from top), AMIE-POT (third from top), and OIM-FAC (bottom); Note that the simulations are not sampled along the satellite orbits and we use geometric height to interpolate to 400 km altitude.

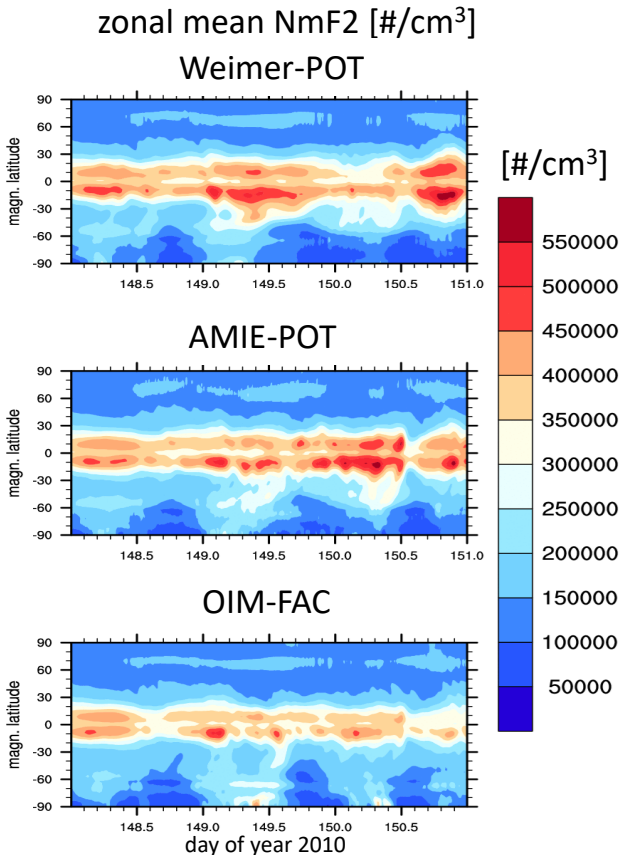

Figure 13. Zonal mean NmF2 $[\#/cm^3]$ over quasi dipole latitude and day of year (doy) 2010 for the simulations Weimer-POT (top), AMIE-POT (middle), and OIM-FAC (bottom).

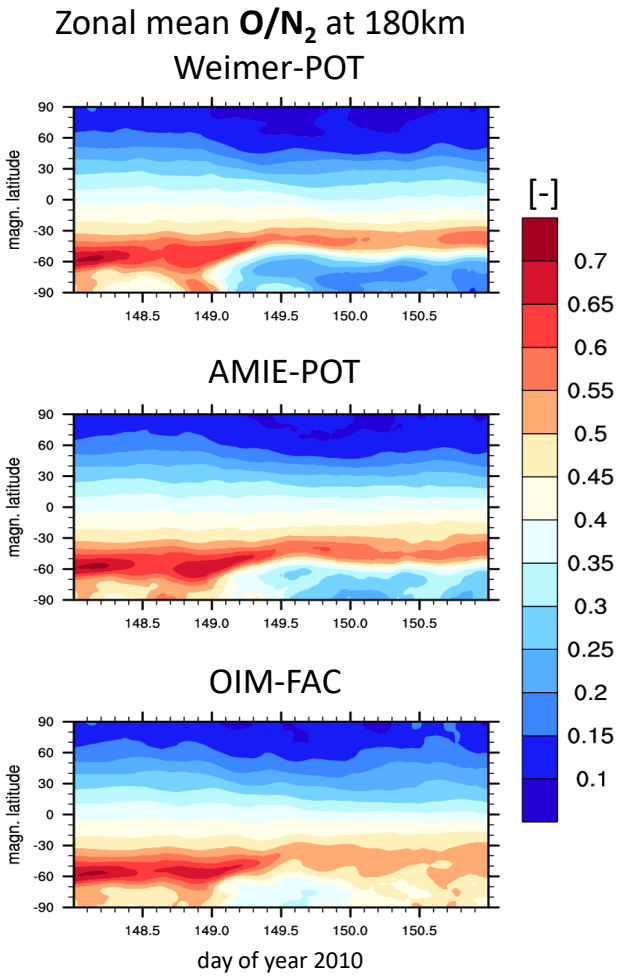

Figure 14. Zonal mean [O]/[N_2] at 180 km over quasi dipole latitude and DOY 2010 for the simulations Weimer-POT (top), AMIE-POT (middle), and OIM-FAC (bottom).

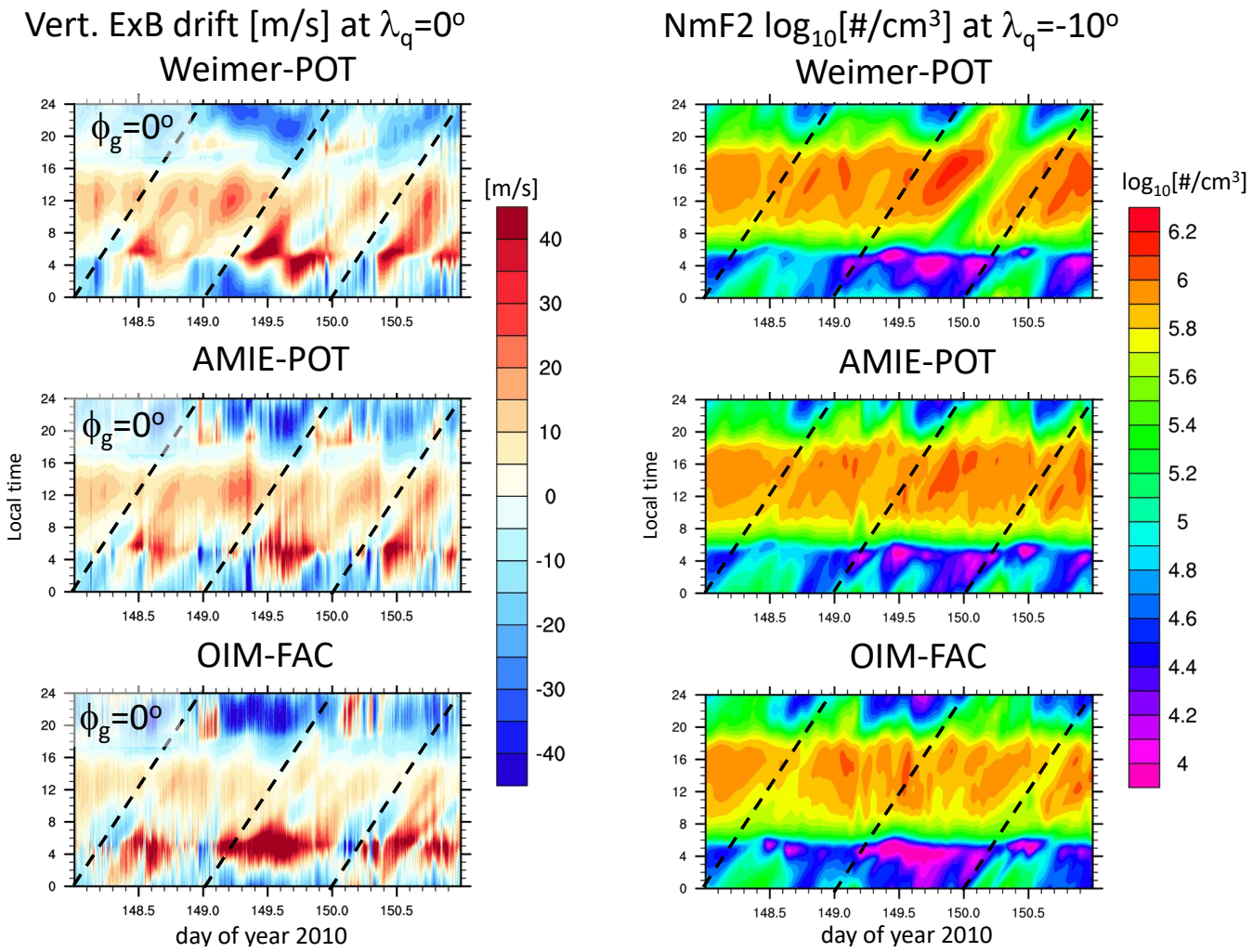

Figure 15. Vertical ExB drift [m/s] at the magnetic equator in the F-region (approximately 215 km) (left panels) and NmF2 log_{10} $[\#/cm^3]$ at quasi dipole latitude $\lambda_q = -10^0$ (right panels) over local time and day of year (DOY) 2010 for the simulations Weimer-POT (top), AMIE-POT (middle), and OIM-FAC (bottom). The dashed line indicates the solar local time variation of a point at geographic longitude $\phi_g = 0$ at the geographic equator.

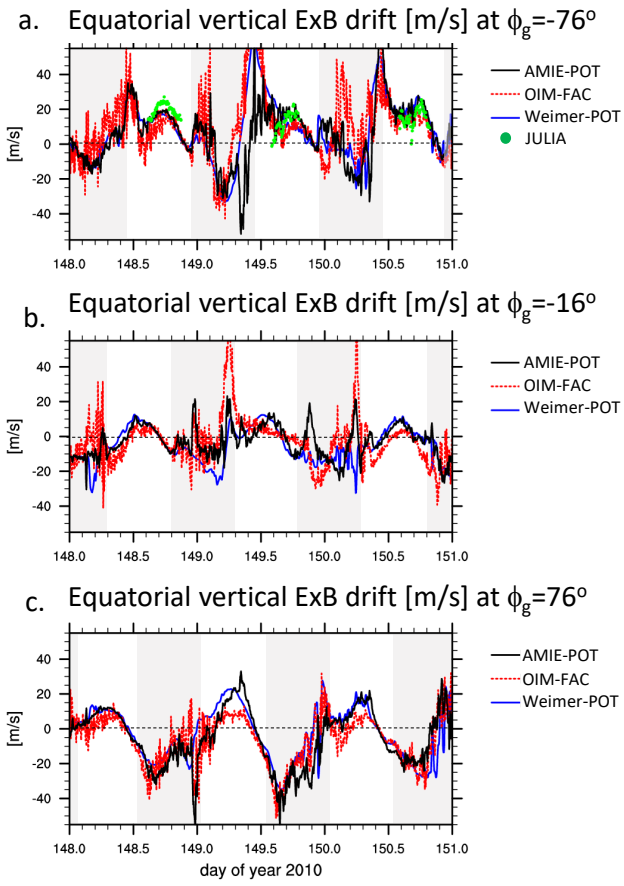

Figure 16. Vertical ExB drift [m/s] at the magnetic equator in the F-region (approximately 215 km) over DOY 2010 for the simulations Weimer-POT (blue), AMIE-POT (black), and OIM-FAC (red) for geographic longitudes a. $\phi_g = -75^o$ (top), b. $\phi_g = -17.5^o$ (middle), and c. $\phi_g = -77.5^o$ (bottom). JULIA observations are illustrated by the green dots. The gray shaded areas indicate 18 to 6 local time.

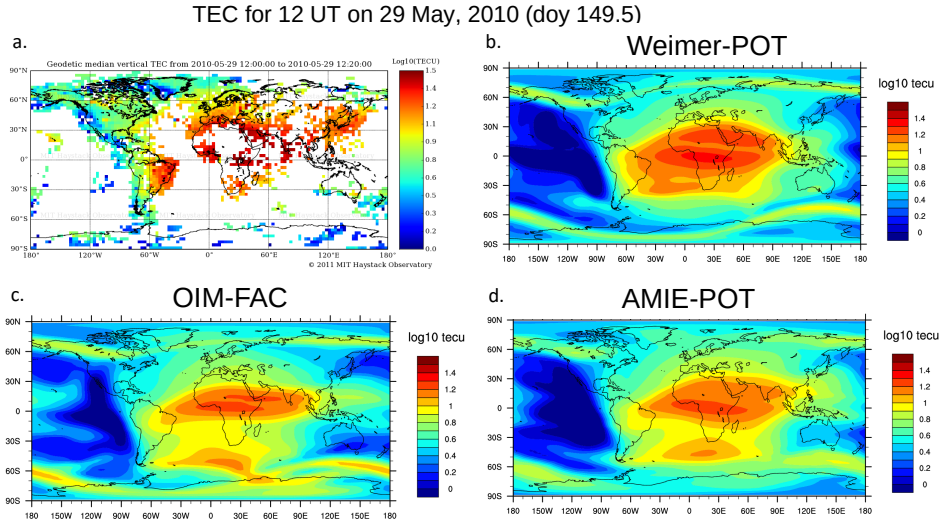

Figure 17. Comparison of total electron content (TEC) at doy 149.5 (29 May 2010 at 12 UT): a. GPS TEC from MIT Haystack observatory, b. Weimer-POT simulation, c. OIM-FAC simulation, d. AMIE-POT simulation.